

Emerging Characterization Techniques for Electrode Interfaces in Sulfide-Based All-Solid-State Lithium Batteries

Feipeng Zhao, Shumin Zhang, Yanguang Li,* and Xueliang Sun*

All-solid-state Li batteries (ASSLBs) are attracting increasing attentions due to their improved safety and high energy density compared with conventional liquid electrolyte-based Li-ion batteries (LIBs). ASSLBs based on sulfide solid-state electrolytes (SEs) is one of the most popular categories, because sulfide SEs have a very competitive ionic conductivity (up to over $10^{-2} \text{ S cm}^{-1}$ at room temperature), medium mechanical stiffness, decent contact with electrode materials, and negligible grain boundary resistance. However, interface problems between electrode materials and sulfide SEs seriously plague the development of high-performance sulfide-based ASSLBs. In-depth understandings on the electrode interface problems are pivotal to propose and explore effective strategies to alleviate those issues. In recent years, diverse advanced characterization techniques have been developed, which deepen insights into the problematic interface from physical, chemical, electrochemical, and mechanochemical perspectives. Herein, electrode interfaces and their fundamental knowledge in sulfide-based ASSLBs are first clarified. Second, various emerging characterizations are overviewed to illustrate the interfacial issues on both oxide cathode/sulfide SE and Li anode/sulfide SE interfaces. Meanwhile, advantages and disadvantages of each characterization techniques are explicated. Finally, an outlook of advanced characterizations that are specifically adapted for interface analysis in sulfide-based ASSLBs is proposed.

1. Introduction

All-solid-state lithium batteries (ASSLBs) have become increasingly attractive due to the improved safety and high energy density compared with conventional lithium-ion batteries based on liquid electrolytes (LEs).^[1] The core component in ASSLBs is the solid-state electrolyte (SE), which predominates the electrochemical performance of ASSLBs.^[2] Generally, there are three kinds of SEs: inorganic SEs, polymer SEs, and inorganic/polymer hybrid SEs. The ionic conductivity is a paramount factor to evaluate SEs, and the improvement of ionic conductivities reflects the advances of developing SEs.^[1c] Among all kinds of SEs, the inorganic SE is a major category, which has experienced a long history of development.^[1b,2b] In the past decade, $\text{Li}_{10}\text{GeP}_2\text{S}_{12}$ (LGPS),^[3] and its families (e.g., $\text{Li}_{9.54}\text{Si}_{1.74}\text{P}_{1.44}\text{S}_{11.7}\text{Cl}_{0.3}$),^[4] as well as the vibrant of Li argyrodites (e.g., $\text{Li}_{6.6}\text{Si}_{0.6}\text{Sb}_{0.4}\text{S}_5\text{I}$)^[5] have achieved excellent room-temperature (RT) ionic conductivities ($>10^{-2} \text{ S cm}^{-1}$) that can be comparable

to LEs. These progresses make sulfide-based SEs receive extensive attention while desolating other inorganic or polymer-based SEs.^[6]

Nevertheless, excellent electrochemical performance of ASSLBs cannot be achieved by just pursuing high ionic conductivities.^[1b-7] There are variety of interfaces in the electrode of ASSLBs, and any one shortcoming of the interface (e.g., contact loss, incompatibility, and reactivity) can significantly affect the battery performance.^[8] Therefore, superior electrode interface is an essential requirement for pursuing high-performance ASSLBs. However, the fact is that electrode interface issues in sulfide-based ASSLBs are pronounced.^[6b,c,8b,9] First, the physical-contact loss takes place at both cathode and Li anode interfaces, although the sulfide SEs are regarded as much “softer” compared with other inorganic SEs (e.g., oxides and halides). One intrinsic reason is the point-to-point contact between the electrode active materials and sulfide SEs, the other one is due to the inevitable volume change of electrode materials during repeatable (de)lithiation.^[10] Second, chemical and electrochemical stabilities of Li/sulfide and oxide cathode/sulfide interfaces are poor because of the narrow electrochemical window of sulfide SEs.^[11] The interfacial products with low ionic conductivity would increase the energy barrier of Li-ion exchange, while

F. Zhao, S. Zhang, X. Sun
Department of Mechanical and Materials Engineering
University of Western Ontario
London, ON N6A 5B9, Canada
E-mail: xsun9@uwo.ca

F. Zhao, S. Zhang, Y. Li
Institute of Functional Nano & Soft Materials (FUNSOM)
Jiangsu Key Laboratory for Carbon-Based Functional Materials and
Devices
Soochow University
Suzhou 215123, China
E-mail: yanguang@suda.edu.cn

Y. Li
Macao Institute of Materials Science and Engineering
Macao University of Science and Technology
Taipa 999078, Macau, SAR, China

 The ORCID identification number(s) for the author(s) of this article can be found under <https://doi.org/10.1002/ssstr.202100146>.

DOI: 10.1002/ssstr.202100146

high-electronic-conductivity component would lead to interminable interfacial decompositions.^[12] Third, mechanochemical instability of Li anode interface against sulfide SEs is found as a non-negligible factor to influence the Li plating and stripping.^[13] Stack pressure is necessary to be applied on the ASSLBs to maintain good contact, but the evolution of the Li anode interface (e.g., surface morphology, voids distribution, cracking, and growth of Li dendrites) depends on the applied pressure and electrochemical conditions (e.g., critical current density [CCD], cut-off capacity during Li symmetric cell cycling).^[10c,14] Overall, all these electrode interface issues impede effective Li-ion transport at the interface, thus deteriorating the electrochemical performance, or even triggering short circuits.^[15]

Understanding these electrode interface issues is urgent in studying sulfide-based ASSLBs, which is also necessary for developing feasible strategies to circumvent the dilemma.^[6b,c,16] The deep analysis and deciphering for the interfacial issues rely on advanced/emerging physical characterization methodologies.^[15a,17] First, observing/tracking the physical contact and distribution of interest chemical species at the interface have been realized using imaging techniques, like optical microscopy (OM) and electron microscopy (EM). Considering the highly reactive and air sensitivity of each component (i.e., Li metal anode, sulfide SEs, and cathode materials) in the sulfide-based ASSLBs, nondestructive imaging techniques spring up. For example, very recently, X-ray tomography (XT) has been reported frequently to study the physical contact (voiding and cracking) caused by uneven Li deposition and mechanochemical instability at the Li/sulfide interface in an operando cell.^[10c,14a] Second, to analyze the chemistry nature of interfacial composition, various spectroscopy-related characterizations have been well developed. X-ray photoelectron spectroscopy (XPS) is one of the most common techniques, which helps to identify the interfacial products at both cathode and Li anode interfaces. The powerful X-ray absorption spectroscopy (XAS) has also been used to excavate the fine structure of interfacial compositions. Furthermore, the interfacial products can be inferred by Raman spectroscopy and time-of-flight secondary-ion mass spectrometry (ToF-SIMS). It is worthwhile noting that corresponding *in situ/operando* techniques (e.g., *in situ/operando* XPS,^[18] *operando* XAS,^[19] *operando* Raman,^[20] and *operando* ToF-SIMS^[21]) have been established to monitor the interface evolution in real time, which are important technologies to track the electrochemical stability.

Herein, we focus on summarizing various emerging characterizations to understand the electrode interface issues deeply in sulfide-based ASSLBs, which is different from existing reviews showing a broad overview on the characterizations on solid-state batteries (SSBs) and interfaces.^[15d,17a–c,e,22] The emerging characterizations present interface issues ranging from the physical interface contact to the (electro)chemically parasitic reactions, delivering an all-rounded insight into the electrode interface of sulfide-based ASSLBs. The organization of this review is schemed as shown in **Figure 1**. First, the fundamental knowledge of interface formation in sulfide-based ASSLBs is introduced, including anode and cathode parts. Second, sorts of advanced characterization methods will be overviewed in detail. Aiming at different objectives, these advanced characterizations will be summarized as two categories: 1) imaging the interface;

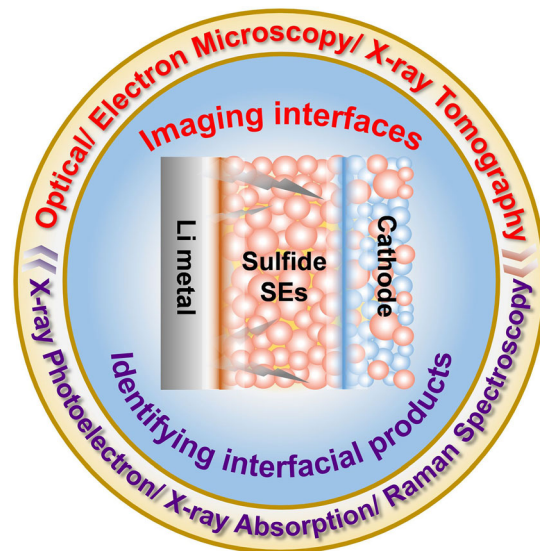


Figure 1. Schematic diagram of the organization of this review paper.

and 2) spectroscopic investigations on the interface. In the first part of imaging techniques, OM, EM (including scanning electron microscopy [SEM] and transmission electron microscopy [TEM]), and XT will be talked about. In the second category, using XPS, XAS, Raman, ToF-SIMS, SXRD, and ssNMR to analyze interface reactions will be overviewed, and the corresponding *in situ/operando* techniques (if applicable) will be included as the focus. Finally, conclusions and outlook of advanced characterizations on the electrode interface of sulfide-based ASSLBs will be proposed.

2. Electrode Interfaces in Sulfide-Based ASSLBs

2.1. Formation of Interfaces

As the core component of sulfide-based ASSLBs, the development of sulfide SEs has experienced a very long history. Various sulfide SEs can be classified into four categories according to the phase composition: glass and glass–ceramic, LGPS-type, Li Argyrodites, and others. (**Figure 2**) Several kinds of sulfide SEs in each type can show ultrahigh ionic conductivity at the level of $10^{-2} \text{ S cm}^{-1}$ at RT, which can be comparable to that of conventional LEs.

However, interfaces are ubiquitous in sulfide-based ASSLBs (**Figure 3a**) due to point-to-point contacts among particles or layers. At the anode side, the layer of Li metal contacts with the pellet of sulfide SEs. The surface of Li metal is not completely flat even without electrochemical cycling, and the point-to-point contact essence of the Li/sulfide interface is the origin to generate Li dendrites (**Figure 3b**).^[15b] In addition, the interfacial side reactions between Li metal and sulfide SEs are serious. Comparatively speaking, the electrode interface is more complicated at cathode side, as shown in **Figure 3c**, because the component becomes pluralistic. The interface issues (e.g., space–charge layer [SCL] effect, interfacial reaction) between oxide cathode materials and sulfide SEs are mostly discussed.

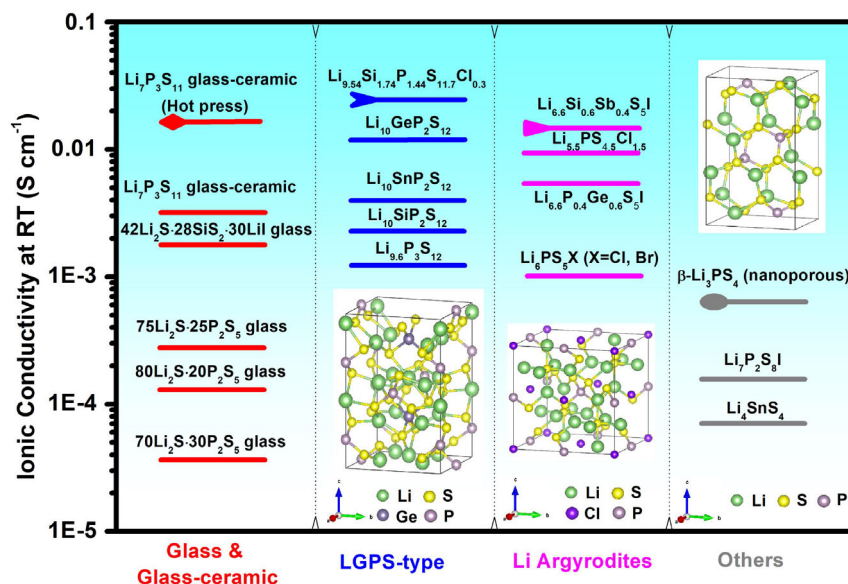


Figure 2. Classification of sulfide-based SEs. The data are collected based on the following references: $\text{Li}_7\text{P}_3\text{S}_{11}$ glass–ceramic (hot press),^[107] $\text{Li}_7\text{P}_3\text{S}_{11}$ glass–ceramic,^[108] $42\text{Li}_2\text{S}\cdot 28\text{SiS}_2\cdot 30\text{LiI}$ glass,^[109] $75\text{Li}_2\text{S}\cdot 25\text{P}_2\text{S}_5$ glass,^[110] $80\text{Li}_2\text{S}\cdot 20\text{P}_2\text{S}_5$ glass,^[110] $70\text{Li}_2\text{S}\cdot 30\text{P}_2\text{S}_5$ glass,^[110] $\text{Li}_{9.54}\text{Si}_{1.74}\text{P}_{1.44}\text{S}_{11.7}\text{Cl}_{0.3}$,^[4a] $\text{Li}_{10}\text{GeP}_2\text{S}_{12}$,^[3] $\text{Li}_{10}\text{SnP}_2\text{S}_{12}$,^[111] $\text{Li}_{10}\text{SiP}_2\text{S}_{12}$,^[112] $\text{Li}_{9.6}\text{P}_3\text{S}_{12}$,^[4a] $\text{Li}_{6.6}\text{Si}_{0.6}\text{Sb}_{0.4}\text{S}_5\text{I}$,^[5b] $\text{Li}_{5.5}\text{PS}_{4.5}\text{Cl}_{1.5}$,^[113] $\text{Li}_{6.6}\text{P}_{0.4}\text{Ge}_{0.6}\text{S}_5\text{I}$,^[114] $\text{Li}_6\text{PS}_5\text{X}$ (X = Cl, Br),^[115] $\beta\text{-Li}_3\text{PS}_4$ (nanoporous),^[26] $\text{Li}_7\text{P}_2\text{S}_8\text{I}$,^[116] and Li_4SnS_4 .^[117] Insets show the schematic diagrams of the unit cells of $\text{Li}_{10}\text{GeP}_2\text{S}_{12}$, $\text{Li}_6\text{PS}_5\text{X}$, and $\beta\text{-Li}_3\text{PS}_4$.

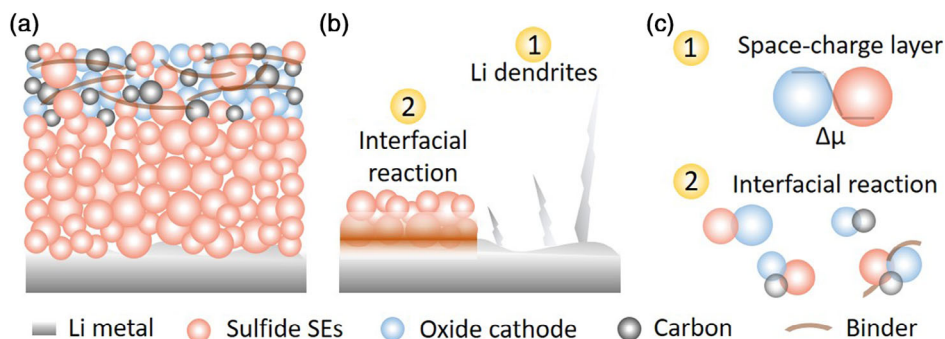


Figure 3. Illustration of the interfacial problems in sulfide-based ASSLBs. a) Schematic diagram of a sulfide-based ASSLB; b) Li metal/sulfide interface issues; and c) oxide cathode/sulfide interface issues.

Moreover, once the carbon conductive agents or binder agents are introduced, bi-phase, triple-phase, or even tetra-phase interfaces would generate to increase the complexity of characterizations. Based on the recent research progresses, interfaces between oxide cathode materials and sulfide SEs are mainly talked about in this review, while binder or conductive-agent effects on the interfaces are excluded.

Fundamentally, the formation of electrode interfaces in solid-state batteries is illustrated in **Figure 4a**, which is driven by the sudden change in the chemical potential of the mobile species (μ_{Li^+}) in SEs and electrodes.^[23] At the anode and cathode interfaces, the difference in chemical potential will generate a driving force for charge reorganization due to the requirement of equilibrating the Fermi energies. At thermodynamic equilibrium, the voltage (V vs. Li/Li^+) is connected to μ_{Li^+} according to $V = -\frac{\mu_{\text{Li}^+}}{qF}$, where F is the Faraday constant. In the generated

interface, the μ_{Li^+} undergoes a drastic variation (several mV nm^{-1}). The low μ_{Li^+} of anode drives mobile cations (Li^+) into the electrolyte and vice versa for the cathode, inducing the depletion or accumulation of charge carriers. By this way, the solid–electrolyte interphase (SEI) at anode and the cathode–electrolyte interphase (CEI) at cathode are generated. Theoretically, the practical electrochemical window can be extended by the rational design of functional interfaces.^[11b] As shown in **Figure 4b**, at the anode side, the interphase consisting of LiX (X = F, Cl, Br, I), Li_2O , Li_2S , Li_3N , or Li_3P products is stable against the Li metal, which is beyond the reduction limit of most SEs. At the equilibrium, the decomposition of the electrolyte (accounting for the formation of anode interface) has no thermodynamic driving force to continue into the bulk. Thus, the electrolyte is stabilized by the decomposition interface. At the cathode side (**Figure 4c**), the coating materials (e.g., LiNbO_3 ,

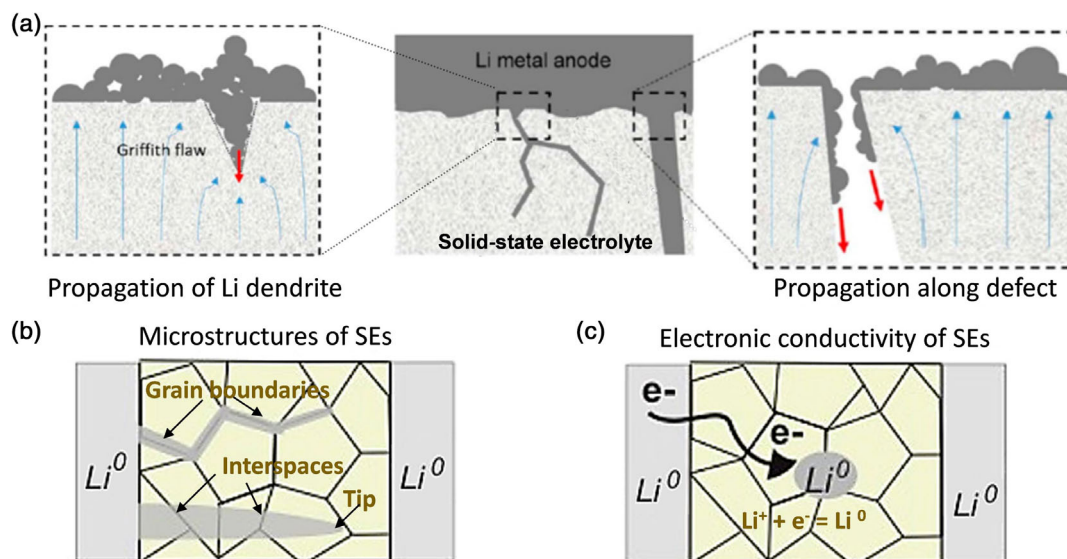


Figure 5. a) Illustration of Li dendrites formation and growth from the Li/SEs interface. Red arrows point toward undesired metal growth into the bulk of SEs and blue arrows show electric field lines. Reproduced with permission.^[28] Copyright 2017, IOP Science. Illustrations of Li dendrites growth due to the microstructures b) and non-negligible electronic conductivity c) of SEs. Reproduced with permission.^[15c] Copyright 2020, American Chemical Society.

hand, the magnified electric field along the edge of interspaces/lithium tips can lead to the charge accumulation, thus causing Li dendrites' growth through the voids in the bulk SEs.^[15d] Finally yet importantly, the non-negligible electronic conductivity of SEs has been demonstrated as an important factor to induce free Li depositions in the bulk electrolytes.^[32]

2.2.2. High (Electro)chemical Reactivity of Li Anode

Due to the strong reducing capability of Li metal, almost every reported sulfide-based SEs can be reduced by Li metal upon electrochemical cycling or even just touching. Zhu et al.^[11b] used computational simulation to determine that the reduction potential of various sulfide SEs is in the range of 1.62–2.28 (V vs. Li/Li⁺, the same hereafter). Several common sulfides, such as Li₃PS₄, Li₁₀GeP₂S₁₂, and Argyrodite Li₆PS₅X (X = Cl, Br, I), show the same reduction potential of 1.71 V, while Li₇P₃S₁₁ even indicates higher reduction potential of 2.28 V. The calculation also suggested that reduction products of sulfides always include insulating Li₃P, Li₂S, and Li halides (e.g., LiCl, LiBr, and LiI) when the sulfide SEs do not contain metal elements, while generating additional metal alloys (e.g., Li–Ge), if there is metal component in the sulfide SEs (e.g., Li₁₀GeP₂S₁₂). These interfacial products have been validated by multiple characterizations, like both ex situ and in situ/operando XPS,^[18,33] operando Raman,^[20a,34] etc., which will be elaborated in the following parts.

2.3. Oxide Cathode/Sulfide SEs' Interface

The reason of the poor cathode interface stability in sulfide-based ASSLBs originates from the SCL effect and low oxidation limit of sulfide SEs.^[8d,11b,23,35] The chemical potential gap between sulfides and oxide cathode materials would cause the formation of

SCL and increase the interfacial impedance. In addition, the low oxidation limit of sulfides leads to severe decomposition of SEs at the cathode interface, thus affecting the interfacial Li-ion transport. It is worth noting that the crystallinity of sulfide SEs can also influence the contact and cathode/sulfide interface stability. Very recently, Wang et al.^[36] reported that contact loss could be mitigated by the glass/glass–ceramic sulfide SEs compared to using crystalline ones. In addition, the crystalline sulfide SEs show higher electronic partial conductivity, which leads to more degradations in the cathode composite.

2.3.1. Space–Charge Layer (SCL) Effect

SCL effect has been frequently reported in the sulfide-based SSBs, which is fundamentally because of the big chemical potential difference between sulfide SEs and commonly used oxide cathode materials ($\mu_{\text{oxides}} > \mu_{\text{sulfides}}$).^[37] Taking the representative β -Li₃PS₄ (LPS) sulfide SEs and LiCoO₂ cathode materials as the example, the movable Li⁺ can transfer from the LPS side to the LCO once these two materials contact with each other.^[35] Due to the mixed conducting feature of LCO cathode materials, the electron would generate to balance the concentration gradient of Li⁺. In this way, the SCL at the oxide side vanishes. However, the Li⁺ in LPS would further transfer to reach an equilibrium state, which can extend the region of SCL at the LPS side and increase the interfacial resistance. The problem of SCL effect can be well alleviated by incorporating one ion-conducting and electron-insulating oxide buffer layer. Ohta et al.^[38] suggested that two interfaces could form when using the buffer layer. One interface is between the mixing cathode oxide material and ion-conducting buffer layer, and the other one is between ion-conducting buffer layer and the sulfide SEs. The formation of thick SCLs is largely suppressed, because 1) there is a similar chemical potential for two oxide layers of the first interface and

2) there are electronically insulated features of the buffer layer and sulfide SEs.

2.3.2. Coating Strategy

As indicated earlier, designing coating materials for cathode particles is the most common strategy to alleviate the cathode interface problems.^[37b] There are several primary requirements for the coating layer: 1) (electro)chemical compatibility with cathode and SEs; 2) high ionic conductivity; 3) low electronic conductivity; and 4) high oxidation limit. Obviously, the (electro)chemical compatibility is the most essential requirement. High ionic conductivity can maintain sufficient interfacial Li^+ transport, while low electronic conductivity and high oxidation limit are required to avoid occurring interfacial reactions. A large number of binary oxide coatings (e.g., ZrO_2 , Al_2O_3 , TiO_2 , SiO_2 , etc.) have been developed as the cathode coating layer to improve the lifespan of conventional LE-based LIBs, but limited binary oxides (except for Al_2O_3 ,^[39] SiO_2 ,^[40] and ZrO_2 ^[41]) can be used for the solid-state counterparts.^[37b] The reason is because the Li-deficient oxide coating cannot provide the necessary Li^+ ionic conductivity at the interface. Therefore, Li-containing ternary oxide coating layers are always required to alleviate the cathode interface problem. A large number of Li-containing oxide coating layers (e.g., Li–Ti–O, Li–Nb–O, Li–Ta–O, Li–Zr–O, Li–P–O, Li–Si–O, and Li–Ti–O) have been reported to improve the cathode interface by decreasing the interfacial impedance and prevent the inter-reaction between cathode materials and sulfide SEs.^[37b] LiNbO_3 (LNO) is the most well-known, because it shows a high ionic conductivity ($10^{-5} \text{ S cm}^{-1}$ level) at RT and a low electronic conductivity of $10^{-11} \text{ S cm}^{-1}$.^[42]

3. Characterizations for Electrode/Sulfide Interfaces

3.1. Imaging Interfaces

The imaging characterization is the most straightforward and intuitive to observe the electrode interface. Depending on the length scale of studying objects, OM and EM are alternatively/conjunctively employed to study the electrode interface issues essentially, including physical contact loss, Li dendrites propagation, microstructure evolution, interlayer/coating effects, etc. In addition, nondestructive XT is emerging to give detailed studies on the Li anode/sulfide interface without disassembling cells. Operando cell configuration can be relatively easily established in XT characterizations, which can provide a real-time monitor on the interfacial issues in a working cell other than earlier mentioned, such as chemomechanical effects (pressure induced) on the Li dendrite growth, interface voiding, SE cracking, and so on.

3.1.1. Optical Microscopy (OM)

OM has been used to monitor the evolution at the interface between Li metal and several representative sulfide SEs, such as glassy $\text{Li}_2\text{S}-\text{P}_2\text{S}_5$ system,^[29a,c] crystalline LGPS,^[29b,43] Li argyrodites,^[43] and polycrystalline Li_3PS_4 .^[29a] The first report was by Chiang and co-workers,^[29a] and the in situ experimental

apparatus is displayed in **Figure 6a**. Two different locations on the glassy $70\text{Li}_2\text{S}-30\text{P}_2\text{S}_5$ pellet were studied to view the Li deposition: one is the so-called “as-fractured surface” (Figure 6b-1), and the other one is “near the precracked area” (Figure 6b-5). In the first area, the author observed Li deposited on the surface of SEs and gradually propagates laterally deviating the tip. There was no cracking or surface degradation, and the cell did not short circuit (Figure 6b-2 to 6b-4). In contrast, in the second area (Figure 6b-6 to 6b-8), there was Li-filled cracking forming and extending into the SE pellet, while there was no Li accumulation on the surface. Apart from the surface image in the case of glassy sulfide, Dasgupta et al.^[29c] further observed the in-plane image of the Li/glassy Li_3PS_4 via operando OM. As suggested in Figure 6c, there were multiply morphologies, namely, straight and spalling, nucleating at the interface of Li/glassy Li_3PS_4 during cell cycling. At the critical current, a sharp increase in overpotential was accompanied with the formation of voids at the interface, and Li penetration took place in the subsequent half cycle, leading to short circuits.

The side reaction between glassy sulfide SE and Li metal cannot be observed by OM imaging intuitively, but the reactive interface between LGPS and Li metal is evident under OM. As shown in Figure 6d, Dasgupta et al.^[29b] found the interface became black after symmetric cell cycling with LGPS SEs, showing that it is increasingly serious along with extending cycling time (10 h). They introduced one Al_2O_3 interlayer by atomic layer deposition (ALD) to reduce the activity of the interfacial reaction. As indicated in the OM image, the dark area was reduced dramatically after experiencing same reaction time compared with the sample without ALD coating. The Li deposition at the surface of polycrystalline $\beta\text{-Li}_3\text{PS}_4$ is different from that of glassy Li_3PS_4 SEs. As reported by Chiang et al.,^[29a] the majority of lithium deposition occurred within the bulk of the $\beta\text{-Li}_3\text{PS}_4$ pellet rather than on the surface. They used the transmission mode of the OM to perform the branching pattern of the deposited Li metal within the bulk of polycrystalline $\beta\text{-Li}_3\text{PS}_4$ pellet (Figure 6e). However, this does not mean Li deposition at the surface of polycrystalline sulfide is uniform, because limited resolution of OM makes the observation restricted at hundreds-micrometer scale.^[44]

3.1.2. Electron Microscopy (EM)

EM, including SEM and TEM, is another commonly used imaging technique to study the interfaces, which can provide high-resolution images beyond the optical diffraction limit. To obtain qualified specimen of interfaces, particularly for TEM measurements, focused ion beam (FIB) is always essential to prepare thin-layer samples.^[45] Furthermore, combination of FIB and SEM (FIB–SEM) is emerging to realize the reconstruction of electrodes, giving out direct observations on cathode/sulfide interface issues. In this section, Li anode interface and cathode interface using EM characterizations are overviewed separately.

At the Li anode side, as indicated in the OM characterization above, the spatial resolution of OM is insufficient to understand the interfacial morphologies, such as micropores, microcracks, or even nanostructures, etc. SEM has been used to compensate for the insufficient resolution of OM in many publications.^[29,46] For example, in the case of Li/polycrystalline $\beta\text{-Li}_3\text{PS}_4$ interface,

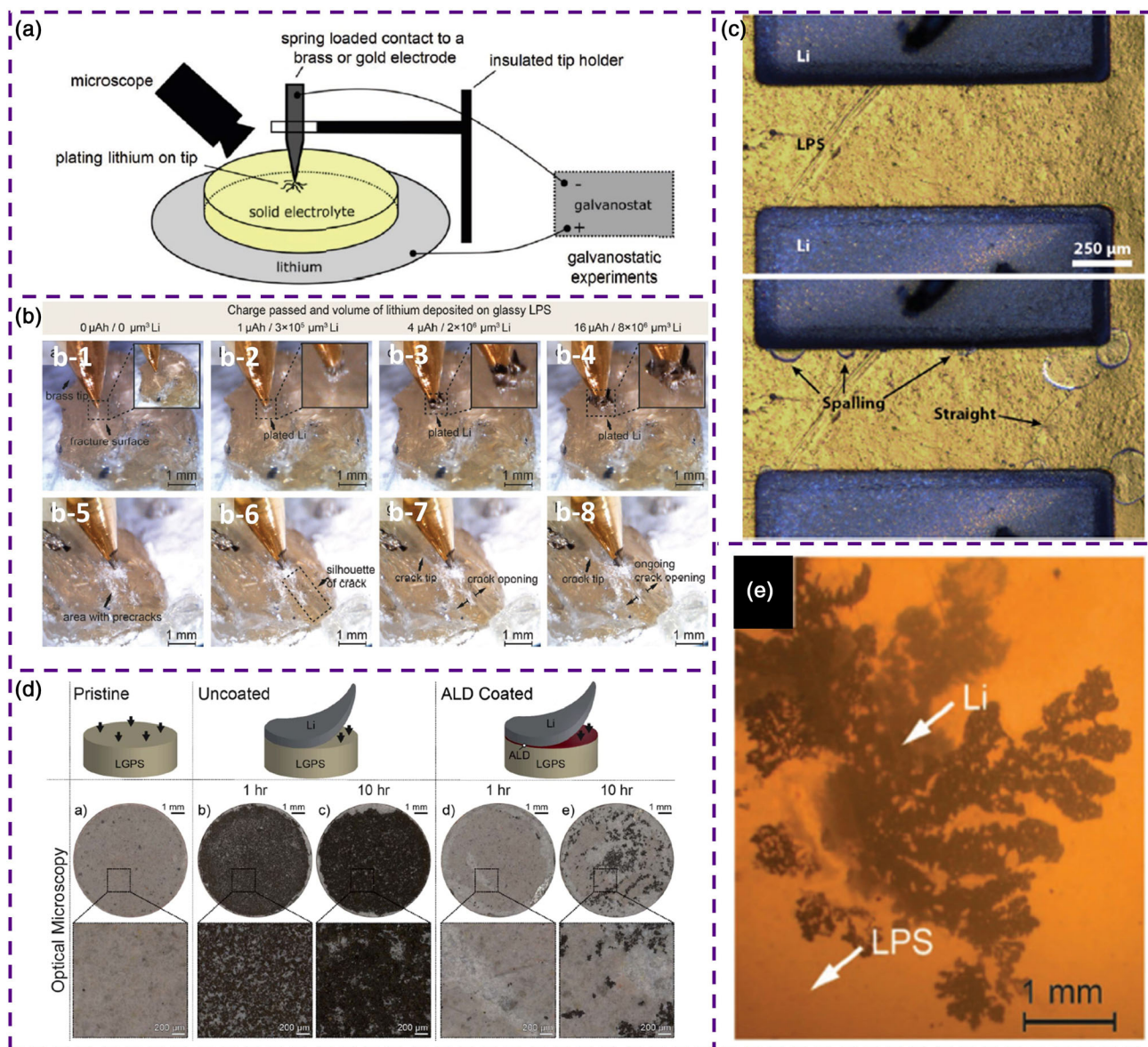


Figure 6. Imaging the Li dendrites at Li/sulfide interfaces with optical microscopy. a) Schematic of apparatus for in situ observation of Li plating on a metal reported by Chiang et al. b) Optical microscopy showing lithium plating onto a brass tip electrode in contact with the glassy SEs. a,b) Reproduced with permission.^[29a] Copyright 2017, Wiley-VCH. c) Operando OM images of in-plane Li/glassy $\text{Li}_3\text{PS}_4/\text{Li}$ cell before and after (down) Li penetration. Reproduced with permission.^[29c] Copyright 2020, Elsevier. d) OM images of the LGPS surface before and after contacting with Li metal with and without ALD coating. Reproduced with permission.^[29b] Copyright 2020, Royal Society of Chemistry. e) Lithium metal deposition at high current density ($\approx 50 \text{ mA cm}^{-2}$) propagates into densely pressed polycrystalline $\beta\text{-Li}_3\text{PS}_4$. Reproduced with permission.^[29a] Copyright 2017, Wiley-VCH.

using SEM can identify that the electrodeposited lithium metal propagated in a cellular manner, and the Li growing direction was along the pore channels, grain boundaries, or both, which were constructed based on the polycrystalline sulfide particles.^[29a] A large number of SEM studies on the anode/sulfide interface focus on the Li deposition and dissolution, and the first-case study using in situ SEM was first reported by Tatsumisago and co-workers.^[46a] As shown in Figure 7a-1, through a tilt of the stage at 30° , the interface between SS

electrode (SS: stainless steels) and $80\text{Li}_2\text{S}-20\text{P}_2\text{S}_5$ glass-ceramic pellet could be observed upon Li plating/stripping. During plating at 2 mA cm^{-2} , the Li penetration proceeded only at the precracked positions, and further growth of Li metal toward SS led to short circuit eventually (Figure 7a-2 and Figure 7a-3). The authors also investigated the influence of applied current density to the morphology of deposition and dissolution of Li metal. The pillared Li deposit after cell short circuiting at 2 mA cm^{-2} is shown in Figure 7a-4, which can

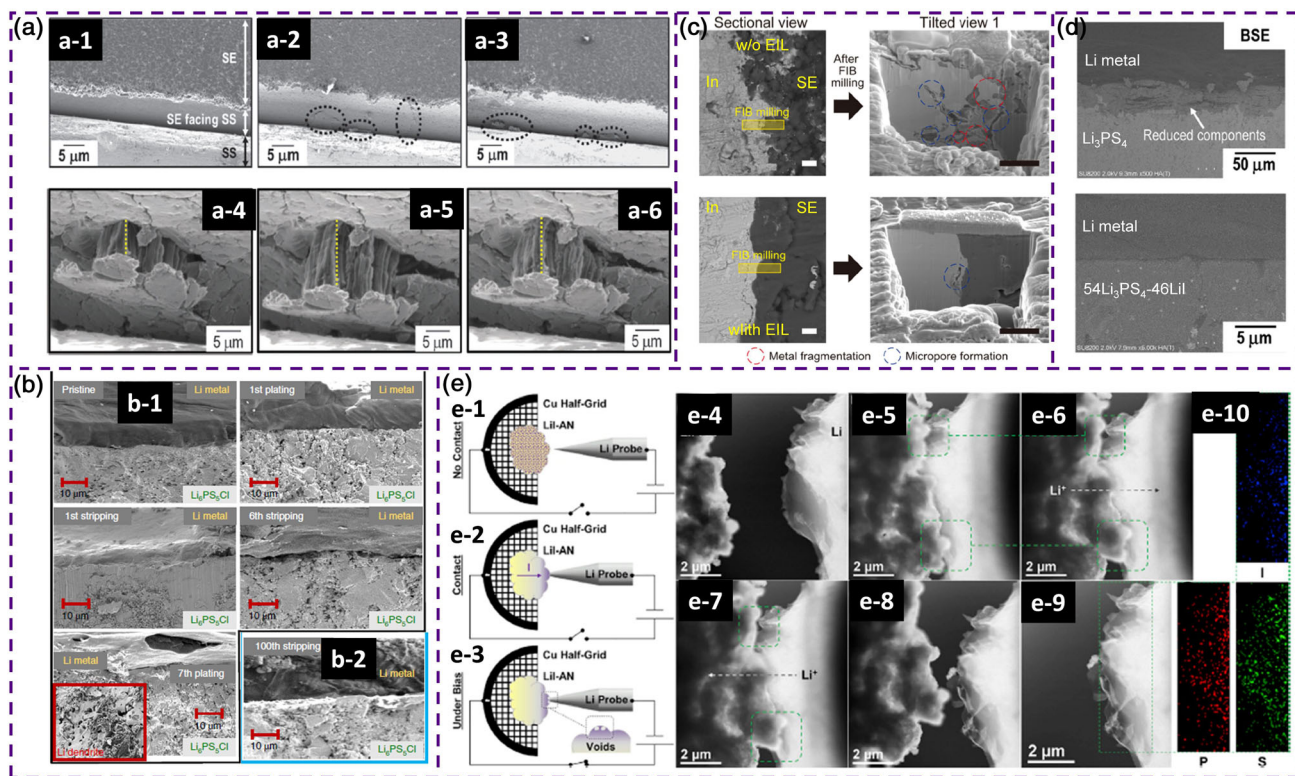


Figure 7. EM characterizations for the Li/sulfide interface. a) SEM images of the interface between the SE layer and SS of the same cell before and after lithium deposition. Reproduced with permission.^[46a] Copyright 2013, Royal Society of Chemistry. b) SEM cross-section images of the Li metal/Li₆PS₅Cl interface at various currents and cycle numbers. Reproduced with permission.^[30a] Copyright 2019, Springer Nature. c) Sectional SEM images after 20 cycles at the anode/Li₆PS₅Cl interface with and without EIL. All scale bars correspond to 5 μm. Reproduced with permission.^[47] Copyright 2020, Elsevier. d) Cross-sectional BSE images of the Li/Li₃PS₄ and Li/54Li₃PS₄-46LiI interfaces after cycling tests at 100 °C. Reproduced with permission.^[48] Copyright 2018, Elsevier. e) In situ TEM observation and analysis on the Li/sulfide interface. Reproduced with permission.^[30b] Copyright 2020, Elsevier.

continue growing and shrinking by further increasing the plating current and stripping current, respectively (Figure 7a-5 and 7a-6). This result indicated that the reversible volume change caused by the reversible Li deposition and dissolution can be accommodated by the 80Li₂S-20P₂S₅ glass-ceramic SE, which is important for applications. Bruce and co-workers^[30a] employed SEM to observe the cross section of Li/Li₆PS₅Cl to reveal the behavior of voiding and Li dendrite growth during Li plating/stripping with various stack pressures. As shown in Figure 7b-1, there were some voids after the first stripping, and they became sizable after the end of sixth stripping. The authors indicated that creep rather than diffusion dominated the rate of replenishing Li at the interface, and the void could generate if the removed Li could not be replenished immediately. Therefore, the applied pressure is important for sulfide-based ASSLBs. Figure 7b-2 shows no evidence of voiding at the end of 100th stripping, which was the result of using 2.5 times higher stacking pressure (7 MPa) compared with the cell in Figure 7b-1 (3.5 MPa). Kim et al.^[47] reported that the interface problem (voiding and Li fragments) between In metal and Li₆PS₅Cl in full cells can be suppressed by introducing one elastic interface layer (EIL): (Li₂S)_{0.75}(P₂S₅)_{0.25} glass. As shown in Figure 7c, FIB milling was carried out on the interface of one cycled cell. There was severe interfacial deterioration with the formation of micropores

and metal fragments at the Li-deposited anode interface without EIL, which was similar to the voids' generation and contact loss classified by Bruce's group.^[30a] Interfacial side reactions and protective effects of the Li/sulfide interface also have been observed with backscattered electron (BSE) imaging of SEM measurements.^[29a,48] As shown in Figure 7d, after galvanostatic cycling tests at 100 °C, the formation of reduced species can be clearly observed. The authors claim that Li₃PS₄ glass decomposed into Li₂S and Li₃P, which could cause large volume expansion (≈150%) and interfacial morphology change. In contrast, the interface was stabilized by adding LiI to the Li₃PS₄ glass (54Li₃PS₄-46LiI), which effectively prevented the side reaction with Li metal and helped maintain a close physical contact during Li dissolution/deposition.^[48]

In addition to SEM, powerful TEM analysis has been conducted to study the Li/sulfide interface at nanoscale. Recently, Hatzell and co-workers^[30b] revealed the transformation of Li/Li₃PS₄-LiI interface during Li plating/stripping via in situ TEM. As shown from Figure 7e-1 to 7e-3, Li metal was placed on a metal probe, while the SE (LiI-AN, representing LiI-incorporated Li₃PS₄ SE) was mounted on a Cu TEM half grid. Figure 7e-4 and 7e-5 reflect the high-angle annular dark-field scanning TEM (HAADF-STEM) images of Li probe and SE prior to and upon contact, respectively. When a reducing bias was

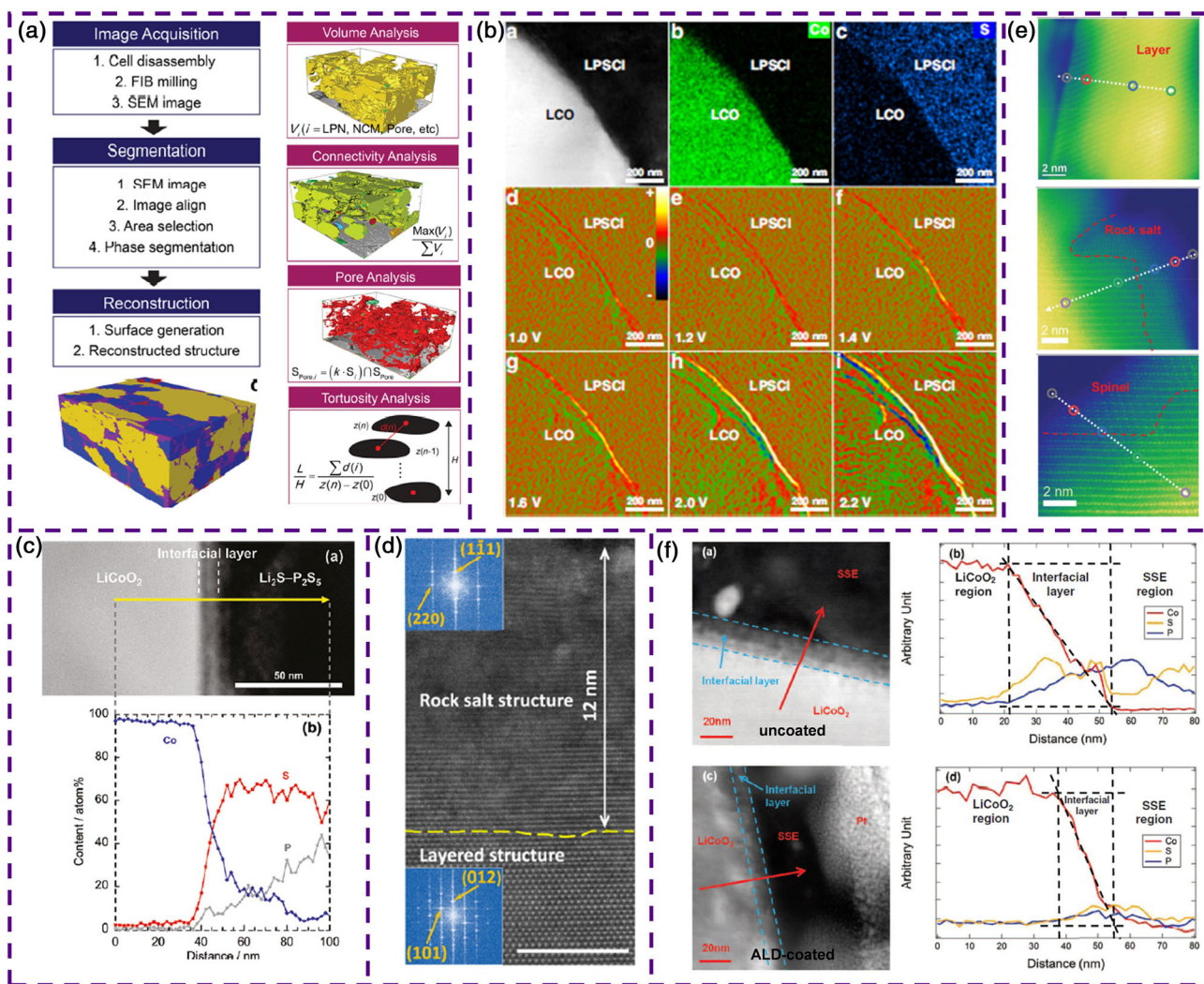


Figure 8. EM characterizations for the cathode/sulfide interface. a) Flow diagram for quantitative analysis using 3D FIB–SEM reconstruction technique, and the schemes showing multiple analyses from the reconstruction image. Reproduced with permission.^[56b] Copyright 2018, American Chemical Society. b) HAADF-STEM images and element mapping of the LCO/LPSCI interface and in situ DPC-STEM observations of net-charge-density accumulation at the LCO/LPSCI interface with various bias voltages. Reproduced with permission.^[37c] Copyright 2020, Springer Nature. c) Cross-sectional HAADF-STEM image of LCO/Li₂S–P₂S₅ interface after initial charging and EDS line profiles. Reproduced with permission.^[57] Copyright 2010, American Chemical Society. d) Atomic-level STEM-HAADF image of a bare NMC811 cathode after cycling with corresponding FFT patterns inset. Reproduced with permission.^[19b] Copyright 2019, American Chemical Society. e) HAADF-STEM images of SC-NMC532 (single crystal) before and after cycling. From top to down: pristine bare NMC532, bare NMC532 after cycling, and LNTO-coated NMC532 after cycling. The sulfide SE is LGPS. Reproduced with permission.^[60a] Copyright 2021, Wiley-VCH. f) HAADF-STEM images of uncoated and ALD-coated LCO/Li_{3.15}Ge_{0.15}Po_{0.85}S₄ SE interface after cycling, as well as the corresponding EDS line scan in the direction along red arrows. Reproduced with permission.^[39] Copyright 2012, IOP Science.

applied to LiI–AN, Li metal was deposited on the Li probe, when a void/pore formed in the SE region in contact with the Li probe (Figure 7e-6). This void/pore was irreversible and remained after Li was stripped from the probe (Figure 7e-7). After one Li plating and stripping cycle, evidence of Li detachment from the SE could be found from Figure 7e-8. The authors also employed EDS mapping to find that the iodine diffused from SEs to Li metal after Li plating/stripping rather than just be restricted to the physical contact area (Figure 7e-9 to 7e-10). It is recognized that I-rich SEI plays an essential role to improve the Li meal compatibility toward sulfides.^[49]

At cathode/sulfide interface, SEM is one of the inevitable techniques to know the interfacial physical contact. It is a long-standing issue to realize imitate interfacial contact between cathode active materials (CAM) and sulfide SEs. Through SEM measurements (FIB milling is required to obtain high-quality specimen), researchers have verified that the physical contact in the cathode before battery cycling can be improved using a liquid-assistant process,^[50] dry-powder coating,^[51] evaporation coating,^[52] or other advanced interface modification techniques.^[53] However, it is still challenging to maintain good cathode–SE contact after long-term repeatable (de)lithiation.^[54] Using

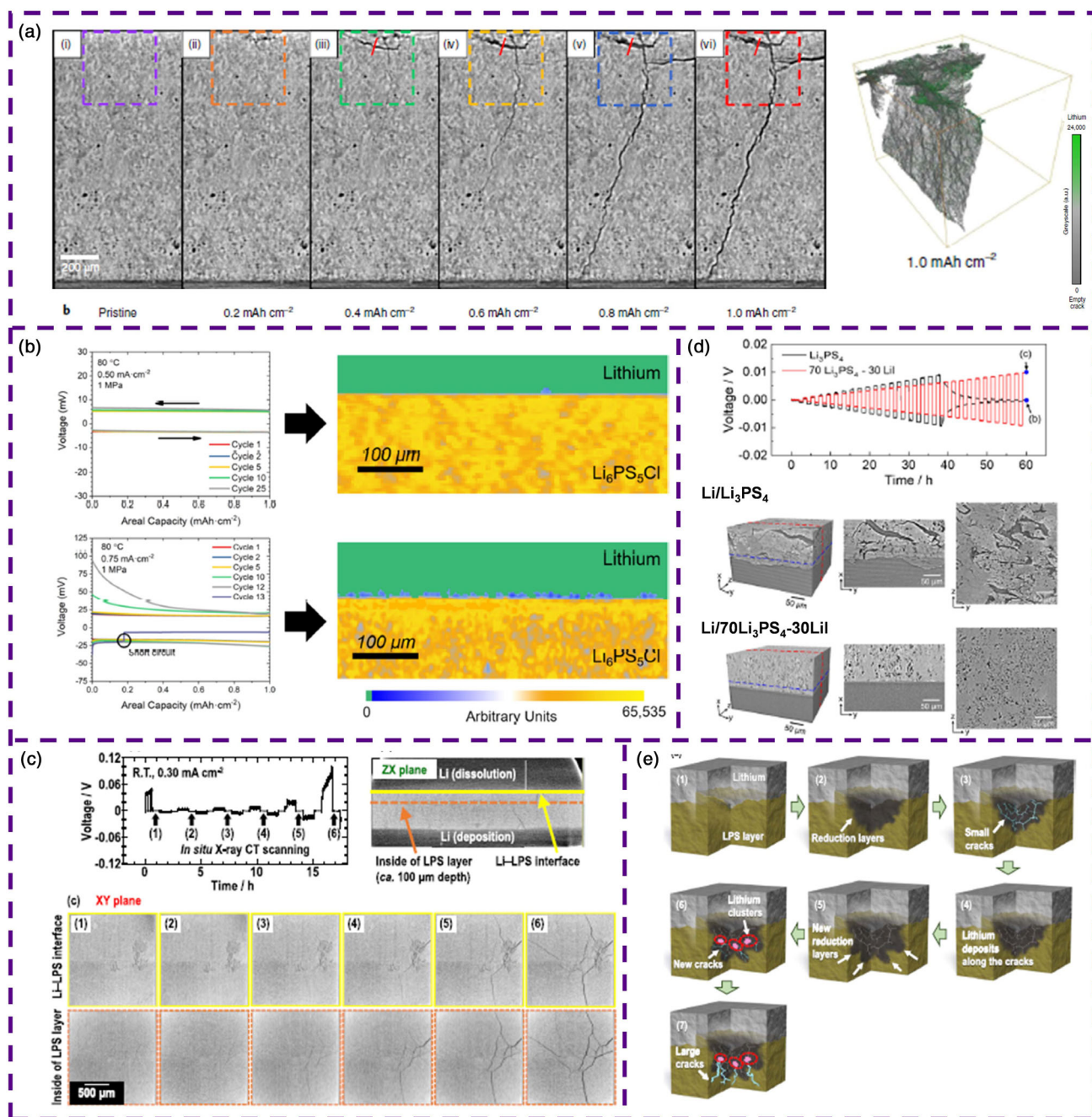


Figure 9. XT characterizations for the Li/sulfide interface. a) In situ phase-contrast XT virtual cross sections during a single plating of a Li/Li₆PS₅Cl/Li cell and analysis of lithium deposition in the cracks. Rendering of a segment of the cell after charging of 1 mAh cm⁻² is also presented. Reproduced with permission.^[14a] Copyright 2021, Springer Nature. b) Li/Li₆PS₅Cl/Li symmetric cells cycling at 80 °C under 1 MPa at 0.5 mA cm⁻² (upside) and 0.75 mA cm⁻² (downside) and corresponding XT cross-sectional images of the Li/Li₆PS₅Cl interfaces. Green, blue, and orange/yellow indicate lithium, voids, and Li₆PS₅Cl, respectively. Reproduced with permission.^[14b] Copyright 2021, American Chemical Society. c) In situ XT images in XY planes at the yellow solid line and the orange broken line during the cycling of a Li/glassy Li₃PS₄/Li symmetric cell. Reproduced with permission.^[72] Copyright 2021, American Chemical Society. d) 3D volume and cross-sectional XT images of Li/Li₃PS₄ and Li/70Li₃PS₄-30LiI after the cycling of the corresponding symmetric cells. Reproduced with permission.^[74] Copyright 2021, American Chemical Society. e) Crack formation mechanism initiated at the interface between the lithium and sulfide pellet. Red circles indicate Li cluster with low densities. Reproduced with permission.^[72] Copyright 2021, American Chemical Society.

single-crystal CAM is a good strategy to prevent the material cracking after repeatable cycling in the sulfide-based SSBs, which has been recently demonstrated by Yang and co-workers^[55] We

would not overview any more details on these conventional applications of SEM in this review paper. Instead, we will emphasize one emerging SEM-related characterization that is SEM

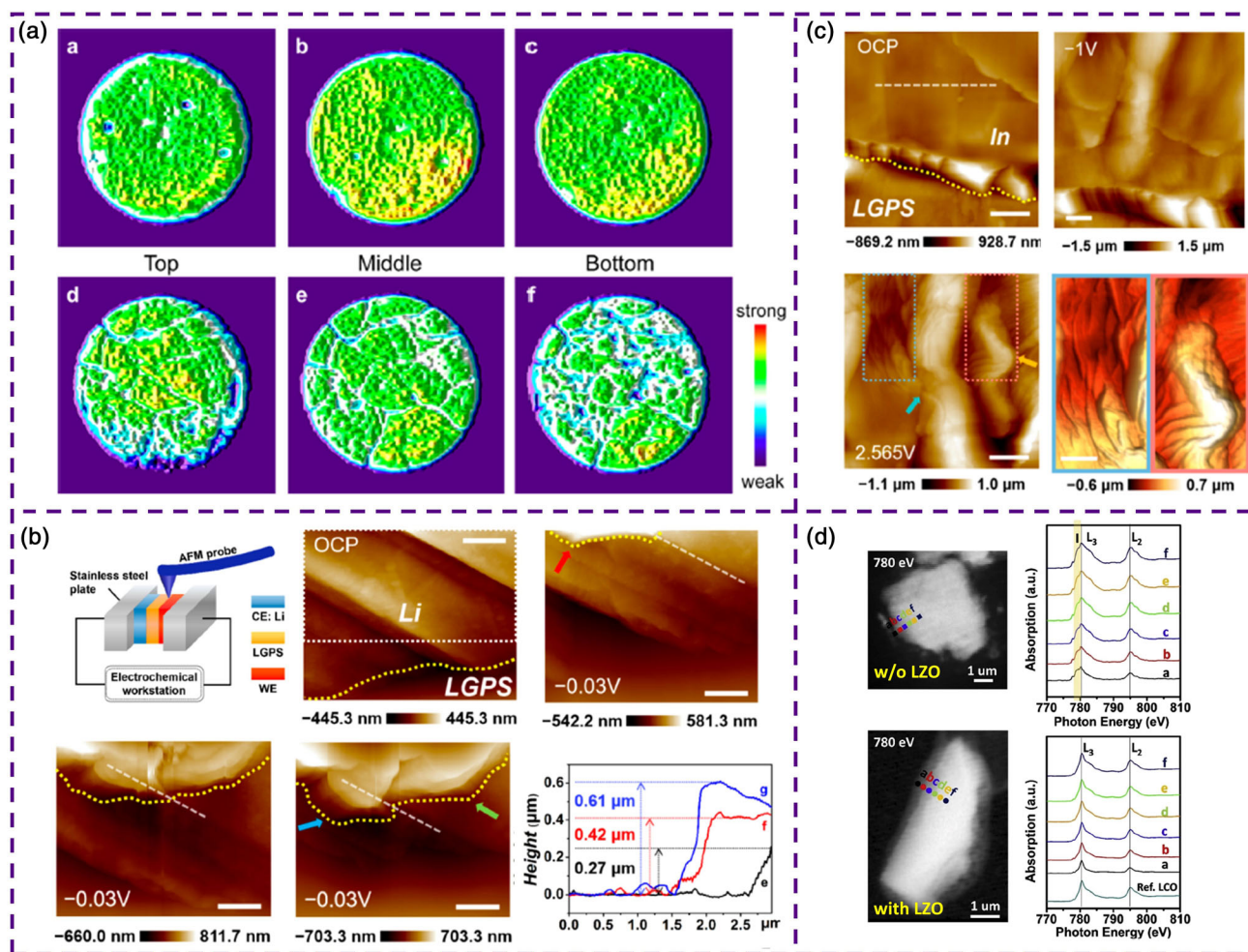


Figure 10. Other advanced imaging techniques to study electrode/sulfide interfaces. a) 2D cross sections taken from 3D ^7Li MRI images of pristine (upside) and cycled $\text{Li}_{10}\text{GeP}_2\text{S}_{12}$ SEs (downside) in a Li-Li symmetric cell. Reproduced with permission.^[75] Copyright 2018, American Chemical Society. b) In situ AFM experimental apparatus and the images of the Li electrodes at open-circuit potential (OCP) and cathodic potential (-0.03 V), as well as the height section profiles of the deposited Li along the white dashed lines. c) In situ AFM images of the In electrode (OCP) and Li-deposited In electrodes at cathodic (-1 V) and anodic (2.565 V) potentials. The 3D AFM images of the wrinkled structures in blue and pink dotted boxes are displayed as well. b,c) Reproduced with permission.^[76] Copyright 2021, American Chemical Society. d) STXM optical density images of single LCO particle after cycling with $\text{Li}_6\text{PS}_5\text{Cl}$ SEs with and without ALD-ZO coating. The corresponding XANES of Co $\text{L}_{3,2}$ edges of the marked areas in images are also provided. Reproduced with permission.^[63b] Copyright 2020, Elsevier.

reconstruction.^[56] This technique could play an important role to present an integrated electrode information with qualitative ability in a 3D manner. The sequence of realizing the characterization is suggested in Figure 8a, consisting of FIB milling, acquisition of consecutive SEM images, and subsequent image segmentation and reconstruction.^[56b] The 3D-reconstruction image is illustrated to indicate solid electrolyte (yellow), CAM (blue), conductive additive (red), and pore (purple). The interested subdivisions can be used to do qualitative analysis on the volume, connectivity, pore, and tortuosity based on theoretical equations.

Incompatibilities at the cathode/sulfide composite originate from the SCL effect and the (electro)chemical activity. These issues usually occur from microscopic down to atomic scale. TEM is a powerful characterization with the highest spatial resolution among all imaging techniques. Furthermore, TEM

can be equipped with energy-dispersive X-ray spectroscopy (EDX) and electron energy loss spectroscopy (EELS), which can provide decent energy resolution to study the atomic composition, chemical bonding, and valence of elements.^[15a] TEM characterizations on the cathode/sulfide interface can be generally divided into two categories: 1) deciphering the interface issue at atomic level and 2) describing the cathode coating layer.

In the first category, Cui and co-workers recently visualized SCL via in situ differential phase-contrast scanning transmission electron microscopy (DPC-STEM) technique. This technique was used to investigate the net-charge-density distribution across the LCO/LPSC (LCO: LiCoO_2 , LPSC: $\text{Li}_6\text{PS}_5\text{Cl}$) interface.^[37c] As shown in Figure 8b, at the bias voltage of 1 V , slightly negative net charge density was indicated on the LCO side of the interface, while positive for the LPSC side. This is corresponding to Li^+

ions extracted from LCO crystal lattices and entering into the interstitials of LPSCL SEs. The difference between negative and positive net charge densities was found increasingly pronounced along with higher bias voltages. This study suggested the first direct experimental evidence of the SCL effect dynamically reflecting Li-ion transport at the cathode/sulfide interface. In addition to the fundamental SCL effect, elements' mutual diffusion and cathode materials' structure change were all observed through TEM. Hayashi and co-workers^[57] utilized EDS line scan for the LCO/80Li₂S–20P₂S₅ interface after cycling to find that P and S diffuse from the LPS side to the LCO particle, while Co was witnessed to diffuse extending to over 50 nm away the bulk LCO (Figure 8c). The mutual diffusion of Co, P, and S was regarded as the main evidence to form interfacial layer, and this layer even existed in the case of using LNO coating for LCO cathode.^[58] Tsukasaki et al.^[59] conducted high-resolution TEM (HRTEM) to observe that the layered crystal structure of NMC111 (LiNi_{1/3}Mn_{1/3}Co_{1/3}O₂) became partially amorphous at the NMC111/glassy 75Li₂S–25P₂S₅ interface after cycling. Sun and co-workers^[19b] performed HAADF-STEM combined with fast Fourier transformation (FFT) to witness the transition of NMC811 (LiNi_{0.8}Mn_{0.1}Co_{0.1}O₂) from the typical layered structure to rock-salt phase at the interface of 12 nm (against LGPS) (Figure 8d). This similar phase transition could also be found for the interface between single-crystal LiNi_{0.5}Mn_{0.3}Co_{0.2}O₂ (SC-NMC532) and sulfide SEs without interfacial protection.^[60]

In the second category of describing the cathode coating layer, on the one hand, as the thickness of coating layer is normally nanosized, TEM was required to confirm the morphology and structure of coating layers attached on the cathode materials, such as Li–Nb–O-based,^[19b,61] Li–Nb–Ta–O,^[60a,62] Li–Zr–O,^[60b,63] Li–P–O,^[64] Li–B–O,^[60b] Li–La–Sr–Ti–O,^[65] Li–Co–Ti–O,^[66] Li_xZr₂(PO₄)₃ coating,^[67] etc. On the other hand, the functionality of coating layer was revealed. For example, Sun and co-workers^[60a] reported that LNTO (Li–Nb–Ta–O) coating on SC-NMC532 could effectively suppress the oxygen loss from the cathode to LGPS SE, thus increasing interface stability. They used HAADF-STEM to witness a thin spinel layer (1–3 nm) rather than an undesired rock-salt structure at the near surface of LNTO-coated SC-NMC532 cathode (Figure 8e). The authors further claimed that the spinel structure derived from LNTO coating could mitigate the detrimental interfacial structural change. Lee and co-workers^[39] elucidated that the coating effect can suppress element mutual diffusions, thus reducing the interface thickness. As displayed in Figure 8f, the HAADF-STEM image and EDS line scan of Al₂O₃-coated LCO/Li_{3.15}Ge_{0.15}P_{0.85}S₄ interface clearly show that the interface thickness reduced by ≈50% compared with the uncoated cathode.

3.1.3. X-Ray Tomography (XT)

Li anode/sulfide interface is sensitive to air due to the high reactivity of Li metal and sulfide SEs; therefore, characterizations on Li/sulfide interface required high standards of inert atmosphere and thermal control to keep the interface indestructible. OM and EM-based characterizations have been overviewed to analyze the dendrite issue through elaborately preparing the specimen by FIB milling or designing in situ/operando experimental

apparatus. However, it is still challenging to realize nondestructive analysis via these characterizations, particularly for detecting veritable interface situations in an operating cell. XT is one indispensable imaging technique that can capture the real interior of one cell without disassembling cells. The used X-ray can be generated with laboratory-based or synchrotron radiation (SR) source, while synchrotron-based XT can provide higher spatial resolution and higher scan rate.^[68] In XT, depending on the element, denser materials with high-Z elements (e.g., sulfide SEs) attenuate the X-rays more than low-Z elements (e.g., Li metal, and gas). Therefore, darker regions highlighted in the tomogram and 3D-reconstructed image will be identified as voids/cracks/dendrites.

Implementing XT to visualize the Li/sulfide interface is relatively new compared with other imaging techniques, and the early studies were conducted by Pylypenko and co-workers and Sun et al.^[69] They visualized the interfacial morphology change at interfaces of Li/β-Li₃PS₄ and Li/Li₁₀SnP₂S₁₂ in operando studies, respectively. Their work has inspired more research in this field, including explaining the formation (initiating from the Li/sulfide interface) and growth mechanism of Li dendrites,^[10c,14,30a] observing that the Li dendrites in bulk SEs resulted from different stack pressures,^[70] and analyzing the porosity of the bulk SE pellet before and after electrochemical reactions.^[30b] Among which, the interface-related XT characterizations are what we focus on in this review paper. One recent XT study performed by Bruce and co-workers^[14a] explained the plating-induced cracking in Li/Li₆PS₅Cl/Li symmetric cells. As displayed in Figure 9a, during plating for one Li electrode, the cross-section images obtained by XT after each electrochemical steps suggested that one crack initiated from the interface (upside) to the other electrode (down side). Although the crack traversed the entire Li₆PS₅Cl layer, the cell was still not shorting. The authors measured grayscale profiles across the crack at the region indicated by the red lines and confirmed that the Li dendrites grew with filling the crack first and the crack propagated ahead of the dendrite penetration. As shown in the 3D image rendering, the Li dendrites were still confined in the crack, while crack had propagated to the bottom electrode. However, this cracking and Li dendrite growth mechanism starting from the Li/sulfide interface were not observed in another XT study for the graphite/Li₃PS₄ interface by Novak and co-workers^[71] The authors explained that the difference is due to the fabrication of cells. During the stripping process for one electrode of the Li/Li₆PS₅Cl Li symmetric cell, Bruce et al. suggested that the voids' formation at the interface was essential to promote the nucleation and growth of Li dendrites, which was explained by SEM characterizations of the stripped Li metal/Li₆PS₅Cl interfaces in the EM section.^[30a] XT was also used to witness the accumulation of voids deviating from the interface to SE layer with increasing plating/stripping cycles, because voids show low X-ray attenuation compared with bulk Li metal anode and SE pellet.^[10c,30a] Bruce and co-workers further explored that the voiding at the interface can be suppressed by increasing the temperature at the same stack pressure.^[14b] Their electrochemical data suggested that CCD for void formation on cycling at the Li/Li₆PS₅Cl interface increases from < 0.25 mA cm⁻² at 25 °C to >0.5 mA cm⁻² at 80 °C under 1 MPa pressure. XT was used

to prove the formation of voids with the critical plating/stripping conditions (Figure 9b).

One drawback of the research above using XT to analyze the Li/sulfide interface is lacking the consideration of interfacial reactions between Li metal and sulfide SEs. Hayashi and co-workers^[72] reported a plausible theory to explain the failure mechanism of Li/sulfide issue by considering the interface side reactions. XT imaging was also used to visualize the crack propagation. As shown in Figure 9c, tomograms of two positions (one is at Li/glassy Li_3PS_4 surface and the other one is in the bulk SEs) at various electrochemical processes demonstrated that the low-density areas near the Li/ Li_3PS_4 interface triggered crack expansion inside the bulk SE. The authors considered the interfacial reaction between Li and glassy Li_3PS_4 as the main reason for crack formation, because tremendous volume expansion ($\approx 150\%$) was induced by the decomposition of Li_3PS_4 at the interface. Incorporating LiI into the Li_3PS_4 SEs has been widely reported to improve Li compatibility.^[73] As shown in Figure 9d, if replacing Li_3PS_4 with $70\text{Li}_3\text{PS}_4-30\text{LiI}$, the 3D volume and cross-sectional images from the XT indicated that crack generation in the case of LiI-incorporated sulfide becomes negligible compared with that in the bulk Li_3PS_4 .^[74] Based on these intuitive results from XT characterizations, Hayashi and co-workers schemed the progress of crack formation and Li dendrites penetration, as displayed in Figure 9e.^[72] Interfacial reaction took place first. Then, electrochemical Li deposition led to the formation of small cracks in the interface layer. Li deposition could be along the small crack and generate a new Li/sulfide interface afterwards. Therefore, new cracks would form inside the SE pellet, which accommodated more Li deposition subsequently. In this way, the Li cluster was formed and then caused the short circuit. The authors concluded the eventual shorting originated from the generation of small cracks in the reduction layer and was triggered by “repeated-reducing, expanding, and cracking” of sulfide SEs. Similarly, McDowell et al.^[10c] used operando CT to visualize the voids’ formation during lithium stripping in Li/ $\text{Li}_{10}\text{SnP}_2\text{S}_{12}$ /Li symmetric cells. They also quantified the loss of contact derived from the interfacial reaction and regarded it as the primary cause of cell failure.

3.1.4. Others (AFM, STXM)

Besides aforementioned imaging techniques that are widely used to study the interface issues of sulfide-based ASSLBs, there are several other characteristic techniques being reported to visualize the electrode interface recently. Hu and others^[75] used noninvasive ^7Li magnetic resonance imaging (MRI) to examine Li distribution homogeneity in LGPS within Li/LGPS/Li symmetric cells. ^7Li MRI and the derived histograms revealed Li depletion from the Li electrode interface and increased heterogeneity of Li distribution upon electrochemical cycling, as displayed in Figure 10a. Atomic force microscopy (AFM) was used by Wen et al.^[76] to obtain new insights into Li deposition at the anode/LGPS interface. As shown in Figure 10b, in situ AFM measurements were conducted on the cross-sectional interface between working electrode (WE) and LGPS SE layer. If using Li metal as the WE, uneven Li deposition was observed, and the height of deposited Li increased with more charges passing.

Furthermore, this chunk-shaped Li deposition was regarded irreversible when stripping voltage was applied. In sharp contrast, if replacing the Li WE with In, much improved Li deposition and dissolution were found, as shown in Figure 10c. The 3D AFM images of the white dotted rectangle indicated a nanofold-like structure at the surface of the Li-deposited LiIn electrode. The authors claimed that the flexible and wrinkled-structure SEI shell could enable the electrode protection and inner Li accommodation upon cycling. One benefit of using AFM or scanning probe microscopy (SPM)-related characterizations is their capabilities to study the local electrical properties of the electrode. Sakuda and co-workers^[77] rationally used SPM and conductive AFM (C-AFM) to measure the resistance and current distribution of the sulfide cathode composition, respectively. They found that the poor conduction locally limits the charge–discharge reactivity of CAMs, which originated from the poor and uniform interface contact between sulfide SEs and CAM particles. One another advanced imaging technique that should be mentioned is scanning transmission X-ray microscopy (STXM). This imaging technique is a combination of spectromicroscopy, showing decent spatial resolution (30 nm) and high spectral resolution compared with TEM–EELS.^[78] Sun and co-workers^[63b] employed STXM to visualize LCO cathode particles after cycling with and without LZO coating (Figure 10d). According to the X-ray absorption near-edge spectroscopy (XANES) extracted from the designated areas across the interface, LZO coating layer was found to effectively suppress the reduction reaction of Co (+3) in LCO after cycling with $\text{Li}_6\text{PS}_5\text{Cl}$ sulfide SEs.

3.2. Spectroscopic Investigations

Identifying interfacial products is fundamental to understanding the interface issues of both Li anode and cathode in sulfide-based ASSLBs, which benefits to design functional interface (e.g., favorable interlayers) and robust electrolyte composition to prevent the interfacial side reactions and facilitate the interfacial ion transport, thus improving the electrochemical performance. There are various physical characterizations being reported to analyze the interfacial products. In this section, we will review several typical techniques (particularly in situ/operando methods) to show how the interfacial products can be solved via these characterizations.

3.2.1. X-Ray Photoelectron Spectroscopy (XPS)

XPS is ubiquitous tool to be used, because it shows wide accessibility as one lab-based setup and high sensitivity to the surface information of samples. The photon source with a fixed energy is used in conjunction with a hemispherical or cylindrical electron analyzer. For studying the electrode interface in sulfide-based ASSLBs, XPS characterizations, including in situ XPS measurements and XPS depth-profiling analyses, can help to identify the interfacial products in both anode and cathode sides.

At Li anode/sulfide interface, XPS characterizations have been used to detect that sulfide SEs (Li_3PS_4 , $\text{Li}_7\text{P}_3\text{S}_{11}$, $\text{Li}_{10}\text{GeP}_2\text{S}_{12}$, $\text{Li}_6\text{PS}_5\text{X}$, glassy $\text{Li}_2\text{S-P}_2\text{S}_5$) are reduced by Li metal to form Li_2S and Li_3P , as well as LiX ($\text{X} = \text{Cl, Br, I}$) and elemental metal or alloys (e.g., metallic Ge or Li–Ge alloy) for those sulfides with

halogen and metal elements. Two kinds of in situ XPS experimental apparatuses have been elaborately designed to detect the interfacial product between Li metal and sulfides. The first one was developed by Janek et al.^[18a] The schematic diagram of the apparatus is shown in **Figure 11a**, one argon-ion (Ar^+) gun was used to sputter Li metal onto the surface of LGPS pellet via a “bottom-up” approach. After each Li sputtering, XPS measurement was conducted to detect the Li-sputtered LGPS surface. This in situ XPS detected the interfacial products derived from the chemical reactions between Li metal and LGPS. The deconvolution of the XPS peaks indicated the formation of reduced Ge (Ge metal or Li–Ge alloy), Li_2S , and Li_3P formed at the interface. Similar studies were performed to identify the interfacial products between Li metal and other popular sulfide SEs, like glassy $\text{Li}_2\text{S}-\text{P}_2\text{S}_5$,^[79] $\text{Li}_7\text{P}_3\text{S}_{11}$,^[33a] $\text{Li}_6\text{PS}_5\text{X}$ ($\text{X} = \text{Cl}, \text{Br}, \text{I}$),^[80] $\text{Li}_{10}\text{SnP}_2\text{S}_{12}$,^[81] etc. The second in situ XPS experimental apparatus was constructed to detect the interfacial products by electrochemical reactions.^[18b] As shown in **Figure 11b**, during charging process (Li plating), an electron gun bias drove Li^+ migration from the bottom Li electrode to the surface of LPS SEs ($\text{LPS}: 77.5\text{Li}_2\text{S}-22.5\text{P}_2\text{S}_5$) and to complete deposition, while during discharging, UV photons photoionized the deposited Li metal to generate Li^+ and outgoing photoelectron. The resulted accumulated positive charge at the top electrode surface drove Li^+ transport back to the bottom electrode, so the Li metal was stripped from the top electrode. XPS measurements monitored changes at the top surface during Li plating/tripping.

The SEI formed at the interface between deposited Li metal and LPS was irreversible. S and P XPS spectra indicated that the main products of the SEI were Li_2S and Li_3P .

Apart from using conventional XPS to analyze the interface product, depth-profiling XPS was also employed to analyze the chemical composition across the interface. Ar-ion sputter etching on the surface of studied samples followed by XPS measurements helps to realize this. Wang and co-workers^[82] first used depth-profiling XPS to analyze the chemical composition at Li/LGPS interface with and without an interlayer (one nanocomposite) achieved by electrochemical deposition. As shown in **Figure 11c**, unchanged spectra of all elements at the LGPS layer suggested that the reaction between Li and LGPS can be prevented by introducing the interlayer. In the interface, inorganic/organic species and LiF were suggested as the main chemical compositions, which were regarded as the essential role to realize the protection. Compared with the introduction of one additional interlayer, the strategy of modifying sulfide SEs is of high efficiency but of high challenge. Sun and co-workers^[83] reported that fluorinating $\text{Li}_6\text{PS}_5\text{Cl}$ led to the formation of LiF-rich Li anode interface, which could improve the interface and regulate smooth Li plating/stripping. The authors carried out XPS depth-profiling analysis to confirm that a rich LiF-containing interface was formed through the interface and even at the closed Li metal layer (**Figure 11d**), serving as the robust protection layer for the observed ultrastable Li plating/stripping. SR played an important role in the applicability of XPS to

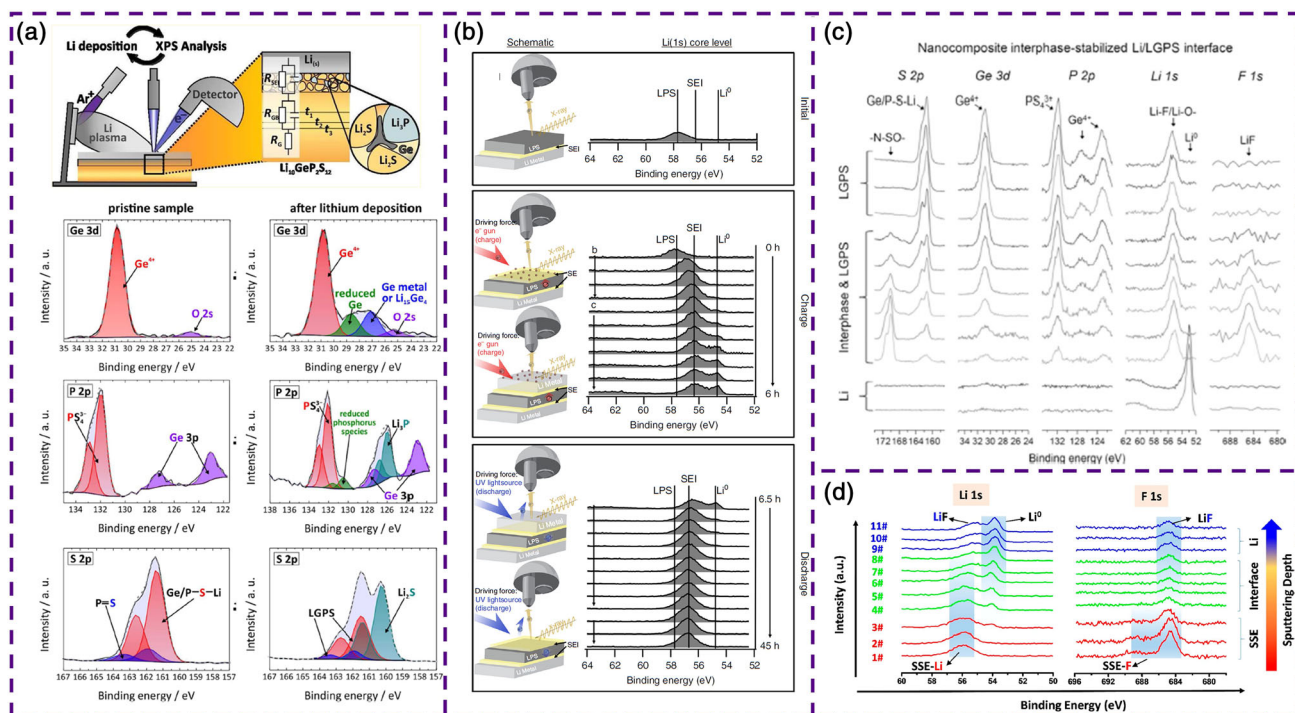


Figure 11. XPS characterizations for Li/sulfide interfaces. a) In situ XPS experimental apparatus developed by Janek et al. XPS spectra of $\text{S } 2p$, $\text{Ge } 3d$, and $\text{P } 2p$ in the pristine LGPS sample and after deposition of 31 nm Li metal. Reproduced with permission.^[18a] Copyright 2016, American Chemical Society. b) Operando XPS schematic and $\text{Li } 1s$ core level evolution. Before and after electrochemical reactions. Reproduced with permission.^[18b] Copyright 2018, Springer Nature. c) XPS depth-profiling analysis for the nanocomposite-stabilized Li/LGPS interface. XPS spectra of $\text{S } 2p$, $\text{Ge } 3d$, $\text{P } 2p$, $\text{Li } 1s$, and $\text{F } 1s$ of the stabilized Li/LGPS interface. Reproduced with permission.^[82] Copyright 2018, Wiley-VCH. d) XPS depth-profiling analysis of the Li metal/fluorinated sulfide interface. Evolution of $\text{Li } 1s$ and $\text{F } 1s$ XPS spectra across the interface. Reproduced with permission.^[83] Copyright 2020, American Chemical Society.

interfacial studies through improving photon flux and energy resolution. Synchrotron-based XPS enables small spot focus from high-brilliance insertion devices and has the ability to change the photon energy, which strongly affects cross section and probing depths. Sun and co-workers^[84] used synchrotron-based XPS to find subtle differences in the interface composition of Li/Li_xSi_y interface tested with increased photon energy from 3 to 6, and 8 keV, corresponding to different depths of X-ray penetration.

At the cathode side, XPS measurements were conducted on the cycled cathode composites to identify the interfacial products. It is noted that depth-profiling analyses were frequently used to preclude the surface contamination, thus detecting real chemical compositions derived from the interfacial reactions. XPS studies that performed on the cathode interface between cathode and various sulfide SEs are multifarious.^[20b,54,58,60a,61b,85] Here, we take promising Argyrodite Li₆PS₅Cl (LPSCl) sulfide SEs as the example to review the XPS studies at LPSCl interface against various oxide CAMs. Dedryvère and co-workers^[86] carried out depth-profiling XPS analysis for the LPSCl interfaces against LCO, LiMn₂O₄ (LMO), and LiNi_{1/3}Co_{1/3}Mn_{1/3}O (NMC111), respectively. S 2*p* and P 2*p* XPS spectra of the LCO/LPSCl cathode composites before and after cycling are shown in **Figure 12a**. Oxidized S and P species were clearly indicated, showing progressive differences at different depths. Etching a 5 or 10 μm-thick layer made the interfacial products of lithium polysulfides (Li₂S_{*n*}), elemental S, P₂S_{*x*} (*x* > 5), and phosphates pronounced. Further check of the Li 1*s* XPS spectra indicated the existence of LiCl in the interface composition.^[33b] In the case of LMO cathode interinterface (**Figure 12b**), the interface products are similar to that of LCO/LPSCl, but these interfacial products already occurred before cycling. This means that chemical reactivity between LPSCl and LMO is more serious larger than that of LPSCl/LCO. As for the LPSCl/NMC111 interface (**Figure 12c**), although there is no big difference between the pristine and the sample after one full cycle, Li₂S_{*n*} and P₂S_{*x*} formed after the first charge. The intensity of these oxidized products after one charge for LPSCl/NMC111 is comparable with the situation of LPSCl/LCO interface after 25 cycles. After long-term cycling (300 cycles), similar observations could be achieved in S 2*p* and P 2*p* spectra compared with LPSCl/LCO and LPSCl/LMO interfaces after 22 and 25 cycles, respectively. Therefore, the authors claimed chemical reactivity of argyrodite LPSCl toward the three CAMs increased in order of: LCO < NMC111 << LMO. Janek and co-workers^[87] analyzed the interfacial products of LPSCl against another popular CAM: LiNi_{0.6}Co_{0.2}Mn_{0.2}O (NMC622). As shown in **Figure 12d**, they not only detected oxidized S and P species (SO_{*x*} and PO_{*x*}) produced at the LPSCl/CMN622 interface but also did careful examination on the O 1*s* spectra before and after cycling. The lattice O of NMC622 almost vanished in the cycled cathode composite, suggesting that the interface layer of the formed interface is thicker than 10 nm, which suppressed the maximum analysis depth of XPS. By means of XPS analysis for LPSCl/NCA cathode composites (NCA: LiNi_{0.85}Co_{0.1}Al_{0.05}O₂), Meng and co-workers^[88] proposed one novel theory of the “self-passivating layer” to hinder the endless interfacial reactions between LPSCl and NCA. They found from the XPS spectra of LPSCl/NCA samples after prolonging cycles (**Figure 12e**) that the new generation rate of interfacial products

(Li₂S_{*n*} and P₂S_{*x*}) became significantly reduced after the first cycle. The authors suggested that electrolyte decomposition was self-terminative, which enabled excellent cycling stability in full-cell cycling. Compared with using XPS studies to disclose the evolution of sulfide SEs in the cathode compositions, insufficient XPS analysis was conducted on the TMs in CAMs after cycling against sulfide SEs. However, there are still several case studies reporting the electrochemical reduction of TMs (Co and Mn) according to the XPS results.^[60a,85]

As we have overviewed above in the imaging section, coating strategies have been widely used to solve the problematic cathode interface toward sulfide SEs. XPS has also demonstrated much improved interface by introducing various Li-containing coating layers.^[63b,64,85,89] Furthermore, the interfacial reaction products associated with adding carbon conductive agents were not revealed by XPS studies.^[90] Various conductive agents with different physical properties (e.g., specific surface area, electronic conductivity) could lead to different degrees of interfacial reactions and then affect the battery performance.

3.2.2. X-Ray Absorption Spectroscopy (XAS)

XAS is an advanced characterization, as the energy source is from a large-scale SR facility and the photon energy is tunable depending on requirements of detection depth, element number of studied objects, etc. X-ray absorption near edge spectroscopy (XANES) and extended X-ray absorption fine spectroscopy (EXAFS) are two subsets of XAS. They are always combined to obtain deep physicochemical information based on elements, such as oxidation states, atomic pair distribution (interatomic distances), coordination numbers, and so on.^[91] Particularly, the chemical evolution of TMs at the interface that are challenging to be well analyzed by XPS can be monitored in the synchrotron-based XAS measurements.

Uchimoto and co-workers^[92] analyzed Co K-edge with depth-resolved XAS to show the protection of Li₃PO₄ interlayer for the LCO cathode materials at cathode interface. As shown in **Figure 13a**, XAS spectra obtained at lower exit angles provide information about the surface of a thin film, while spectra obtained at higher exit angles give information on bulk materials. The author used pulsed laser deposition (PLD) to prepare two thin-film batteries based on 80Li₂S–20P₂S₅ sulfide SEs and LCO cathodes with and without Li₃PO₄ interlayer. XAS measurements were conducted before and after cycling for these two cells. At low exit angles, the negative-energy shift of the whiteline in obtained XANES spectra indicated that Co (3+) was reduced severely at the interface without Li₃PO₄ interlayer (**Figure 13b**), and Co–O bonding distance at the interface was found to be expanded via EXAFS fitting, suggesting local structure change of Co–O bonds in CoO₆ octahedra. In contrast, this expanding phenomenon was not observed at the interface with Li₃PO₄ interlayer (**Figure 13c**). EXAFS fitting was also applied by Li and co-workers^[66] to interpret stabilized interatomic distances of Co–Co, Co–O, and Ge–S at the LCO/LGPS interface with Li₂CoTi₃O₈ (LCTO) interlayer. In addition, in LGPS-based ASSLBs using NMC811 as CAMs, XAS analysis in K-edges of TMs (Ni, Co, and Mn) before and after cycling with and without interface modifications were reported by Sun's

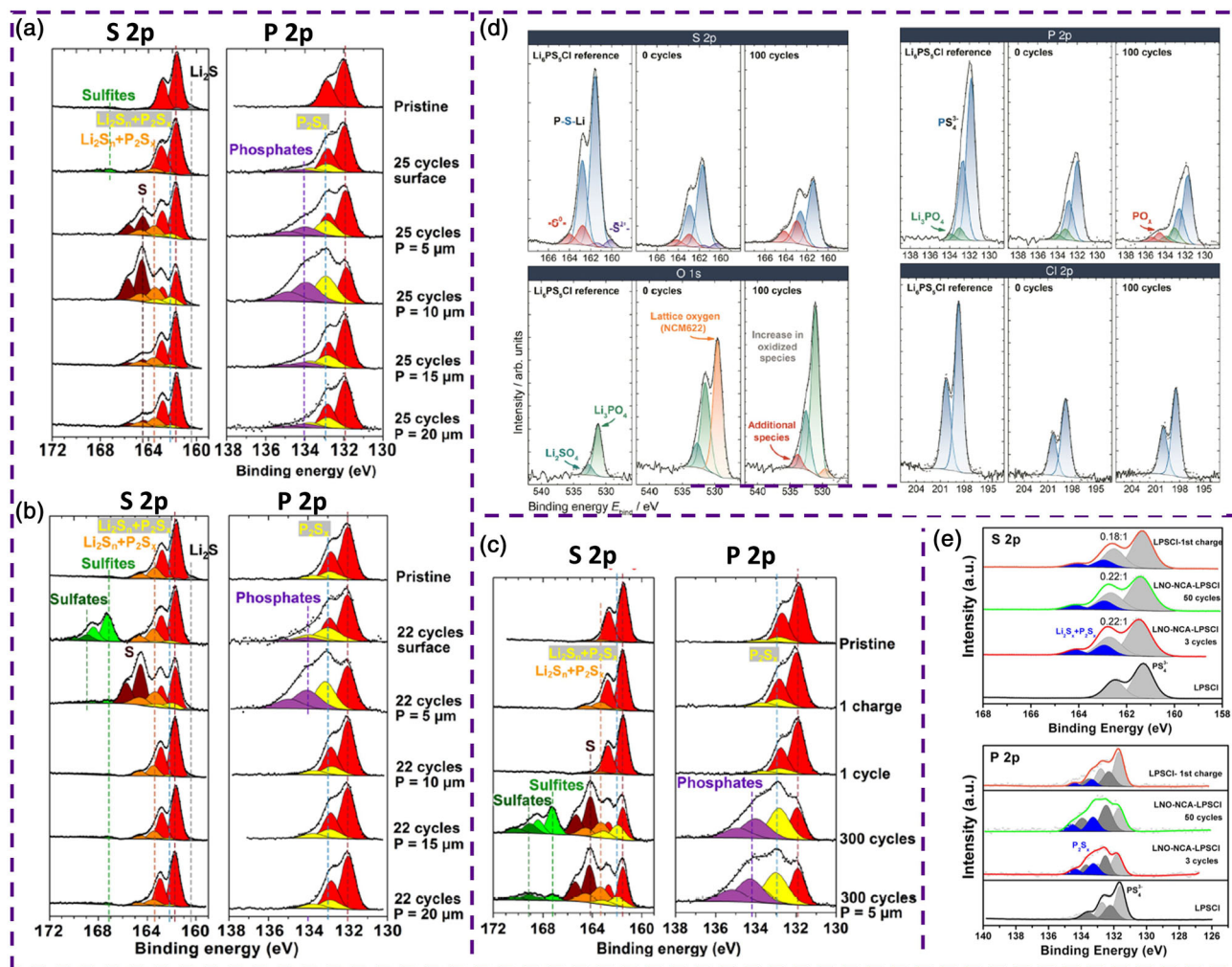


Figure 12. XPS characterizations for interfacial products between $\text{Li}_6\text{PS}_5\text{Cl}$ and various CAMs. S 2p and P 2p XPS spectra of a) LCO/ $\text{Li}_6\text{PS}_5\text{Cl}$; b) LMO/ $\text{Li}_6\text{PS}_5\text{Cl}$; and c) NMC111/ $\text{Li}_6\text{PS}_5\text{Cl}$ cathode composites before and after cycling. Reproduced with permission.^[86] Copyright 2017, American Chemical Society. d) S 2p, P 2p, Cl 2p, and O 1s XPS spectra of $\text{Li}_6\text{PS}_5\text{Cl}$ reference and NMC622/ $\text{Li}_6\text{PS}_5\text{Cl}$ cathode composites before and after cycling. Reproduced with permission.^[87] Copyright 2019, American Chemical Society. e) S 2p and P 2p XPS spectra of NCA/ $\text{Li}_6\text{PS}_5\text{Cl}$ cathode composites before and after various cycles. Reproduced with permission.^[88] Copyright 2019, American Chemical Society.

group.^[19b,64,90d,93] The obvious energy shift of whitelines for TM elements could be largely suppressed by cathode surface coating or cleaning. More importantly, in situ XAS measurement was developed by Sun and co-workers to track the chemical evolution of elements at the NMC811/LGPs interface in electrochemical processes.^[19b] As displayed in Figure 13d, a Mylar film-covered window on the cell allowed the incident X-ray to interact with the cathode composite. XAS spectra of K-edges of P, S, Ni, Co, and Mn could be consecutively obtained during the charging/discharging process. The evolution trend of S K-edge suggested that S at the interface (NMC811/LGPs) converted to Li_2S upon charging but recovered partially in subsequent discharging (Figure 13e). While ALD-LNO coating on NMC811 particles can completely avoid this evolution of S K-edge, demonstrating the interface with coating was stable (Figure 13f). The similar in situ XAS measurement was also used to interpret the LNO coating effect on alleviating interfacial side reactions between LCO and LGPs.^[61b]

3.2.3. Raman Spectroscopy

Raman spectroscopy is the second largest used characterizations underlying XPS to analyze the interfacial products in sulfide-based ASSLBs. It is of high structural specificity and extended sensitivity in the low-vibrational frequency range, which are ideal for pursuing thiophosphate-related structural information.^[94] In collecting Raman spectroscopy, the vacuum chamber is not required; thus, it is relatively easy to design operando cells to track the interface evolution during charging and discharging.

At the anode side, operando Raman measurement was established by Nuzzo and co-workers^[20a] to monitor the interfaces of Li/ $\beta\text{-Li}_3\text{PS}_4$ and Li/LPGS separately, as shown in Figure 14a. During Li plating and stripping toward the Au electrode, partially reversible conversion of PS_4^{3-} to $\text{P}_2\text{S}_6^{4-}$ was found along with the generation of Li_2S at the interface of Li/ $\beta\text{-Li}_3\text{PS}_4$. In addition, the authors found incorporating Si on the anode could facilitate the interconversion between PS_4^{3-} and $\text{P}_2\text{S}_6^{4-}$ during

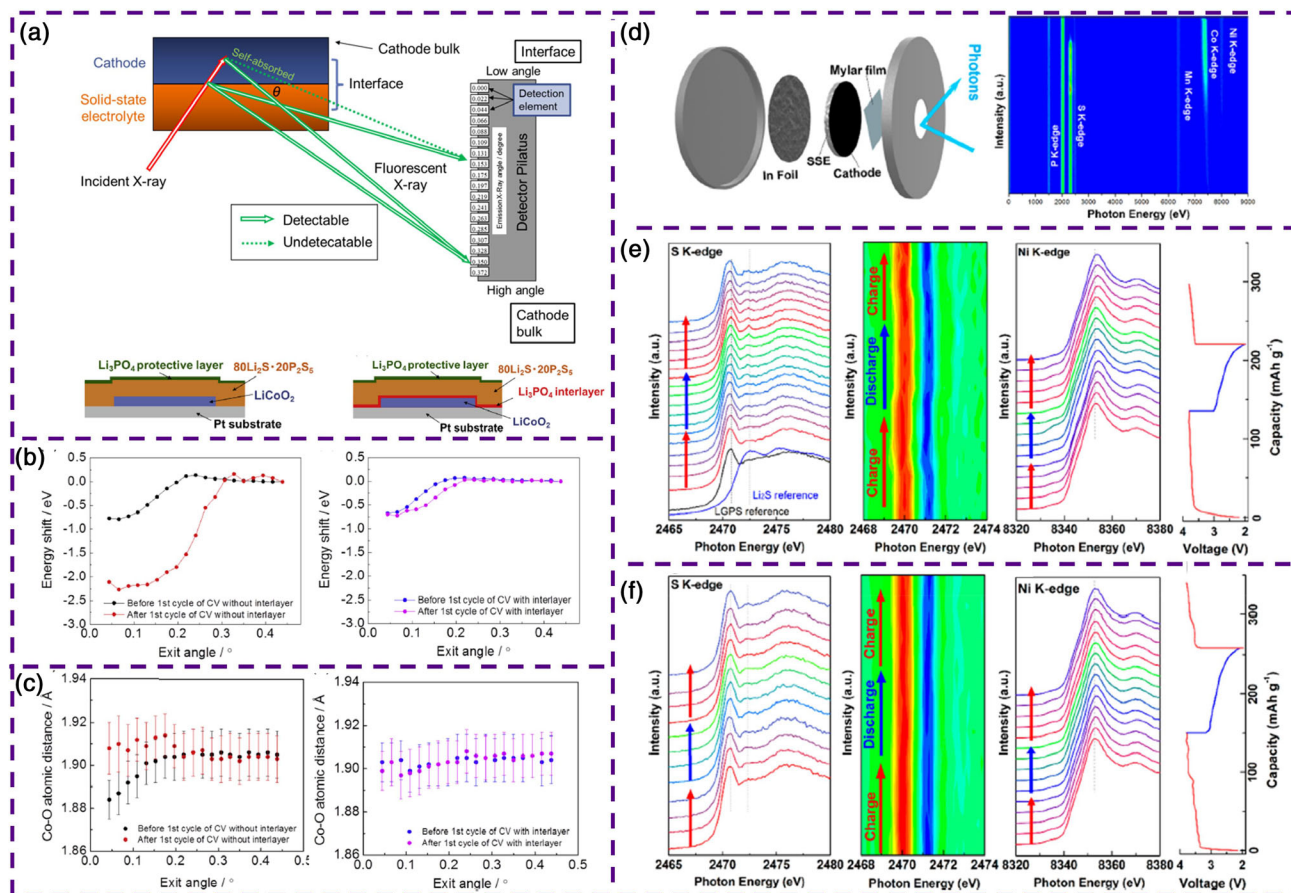


Figure 13. XAS characterizations for cathode/sulfide interfaces. a) Schematic diagram of depth-resolved XAS measurement. b, c) Energy shift at half of the normalized absorbance of XANES spectra from (b) different exit angles and (c) Co—O bond distance derived from the EXAFS fitting for the thin-film electrodes without and with the Li_3PO_4 interlayer before and after the first cycle of CV measurement. Reproduced with permission.^[92] Copyright 2018, Elsevier. d) Schematic figure of the operando XANES cell and obtained Bruker spectrum in a large photon energy region. Operando S K-edge spectra with first derivative mapping, Ni K-edge spectra, and charge/discharge profiles of e) bare NMC811/LGPS and f) LNO-coated NMC811/LGPS cells. Reproduced with permission.^[19b] Copyright 2019, American Chemical Society.

Li plating and stripping.^[34] In contrast, LGPS interface showed irreversible degradation even at the voltage of 0.7 V, which was even prior to effective Li deposition. The authors ascribed this to the high reduction potential limit of LGPS and endless interfacial reaction derived from electron/ion-mixed conducting interface. Recently, Hardwick and co-workers studied the Li/Li₆PS₅Cl interface via operando Raman.^[95] Their results also indicated the formation of Li₂S, while the peak assigned to the PS_4^{3-} did not shift during Li deposition and dissolution but presented a broad feature significantly once bias voltage was applied.

Raman spectroscopy is frequently reported to analyze the cathode/sulfide interface compared with the anode interface studies requiring Li metal. Tatsumisago and co-workers^[96] observed that two fingerprint peaks of LCO (O—Co—O bending: 486 cm^{-1} ; Co—O stretching: 596 cm^{-1}) shifted to a lower wavenumber (due to the expansion of LCO lattice at x -axis) when the cathode was charged in a customized operando cell using glassy $75\text{Li}_2\text{S}-25\text{P}_2\text{S}_5$ SEs (Figure 14b). In addition, one new peak at 675 cm^{-1} could be assigned to generate Co_3O_4 as one interfacial product, which was distributed unevenly in the fully charged

cathode composite according to the mapping of Raman spectra. Hardwick and co-workers evaluated the interfacial products of LCO/Li₆PS₅Cl within a wide wavenumber range.^[95] They found products originating from the decomposition of Li₆PS₅Cl SEs, such as elemental S (at $151, 219, 473\text{ cm}^{-1}$) and P_2S_x ($x = 5$ or 6 or 7 , at 378 and 705 cm^{-1}), which were similar to the in situ Raman results from Cui's group, as shown in Figure 14c.^[67] Actually, Cui et al. dealt with a more intractable problem, namely, improving the interfacial stability between LCO and Li₆PS₅Cl at a high voltage of 4.5 V. They utilized operando Raman to demonstrate the interfacial instability of LCO/Li₆PS₅Cl in a wide voltage range (2.6–4.5 V). Apart from polysulfide and elemental S, they also found CoP_x at 684 cm^{-1} during discharging, which was related to the reduction of P in the Li₆PS₅Cl SEs.^[67] They developed one coating layer (LZPO) to improve the interfacial stability, which was indicated by the stationary contour mapping. In addition, Raman characterizations have also been reported to verify stabilized cathode interfaces (against LGPS SEs), benefiting from LNO coating and element doping.^[97]

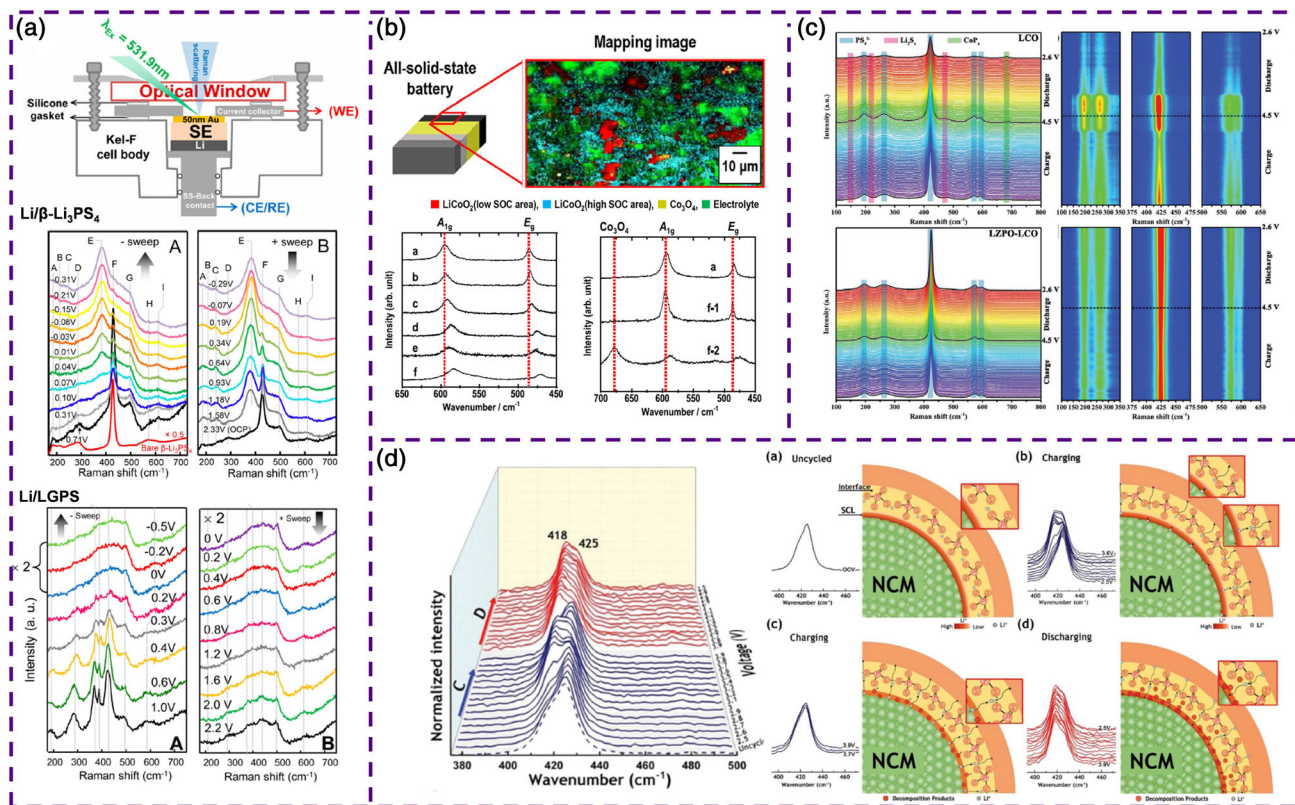


Figure 14. Operando Raman spectroscopy characterizations for electrode/sulfide interfaces. a) Spectroelectrochemistry cell design and Raman spectra to track the interfacial products at Li/β-Li₃PS₄ and Li/LGPS interfaces. Reproduced with permission.^[20a] Copyright 2017, American Chemical Society. b) Schematic diagram of using Ar⁺ milling to obtain the sample and mapping image of the LiCoO₂ electrode layer after the first charging process. The Raman spectra of LiCoO₂ electrode layer at the different charge capacities and different locations after fully charged are also displayed. Reproduced with permission.^[9b] Copyright 2016, Elsevier. c) Raman spectra of Li₆PS₅Cl in LCO/Li₆PS₅Cl (upside) and LZPO-LCO/Li₆PS₅Cl (downside) cathode composites during the charge/discharge process. The corresponding contour maps are also indicated. Reproduced with permission.^[67] Copyright 2021, Wiley-VCH. d) Raman spectra at NCM/Li₆PS₅Cl interface during charging and discharging, and schematic illustrations of interfacial evolution processes based on different vibration states of P—S bond in PS₄³⁻ at NCM/Li₆PS₅Cl interface. Reproduced with permission.^[20b] Copyright 2019, Wiley-VCH.

One another interesting operando Raman characterization linking the interfacial product with SCL evolution at cathode interface of NMC811/Li₆PS₅Cl was recently reported by Zhang et al.^[20b] They found that one new peak (418 cm⁻¹) was adjacent to the fingerprint peak (425 cm⁻¹) of Li₆PS₅Cl and existed all the time during initial charge and discharge. The new peak at 418 cm⁻¹ was regarded as another vibration state of P—S bond in PS₄³⁻, and the authors proposed one plausible theory as displayed in the schematic diagram as shown in Figure 14d. In short, the authors indicated two Li⁺ migration pathways accompanied by the formation of the SCL, which is responsible for the split of the Raman spectra, and the diffusion of decomposition products at the cathode interface brings some fluctuations for the two Raman-peak splits.

3.2.4. Time-of-Flight Secondary-Ion Mass Spectrometry (ToF-SIMS)

ToF-SIMS can analyze informational solid surfaces and thin films by sputtering the surface of the specimen with a focused

primary-ion beam (e.g., Bi³⁺) and collecting and analyzing ejected secondary ions (generally negative-charge fragments). According to the mass/charge ratios of these secondary ions measured with a mass spectrometer, the elemental, isotopic, or molecular composition of the surface can be determined. In addition, sputtering with low-energy ion beam (e.g., Cs⁺) can enable depth-profiling analysis. ToF-SIMS is regarded to possess very high sensitivity toward high-ionization fragments (several orders of magnitude higher than XPS).^[87]

In the field of sulfide-based SSBs, Janek and co-workers first employed ToF-SIMS to analyze the electrochemical degradation of NMC622/LPSCl cathode interface.^[87] As suggested in Figure 15a, due to ion collision (Bi³⁺ beam) on the cathode/sulfide composition, fragments such as MS_x⁻ and MCl_x⁻ (M = Ni, Mn, Co) were generated and detected. The reduced intensity after cycling indicated the local decomposition at the cathode/sulfide interface accompanying the growth of CEI. PO_x⁻ and SO_x⁻ fragments were also suggested as portions of the interfacial products. ToF-SIMS measurements on FIB-cutting samples before and after cycling could clearly reflect that the phosphate fragments were located at the NCM622/sulfide interface (even for the

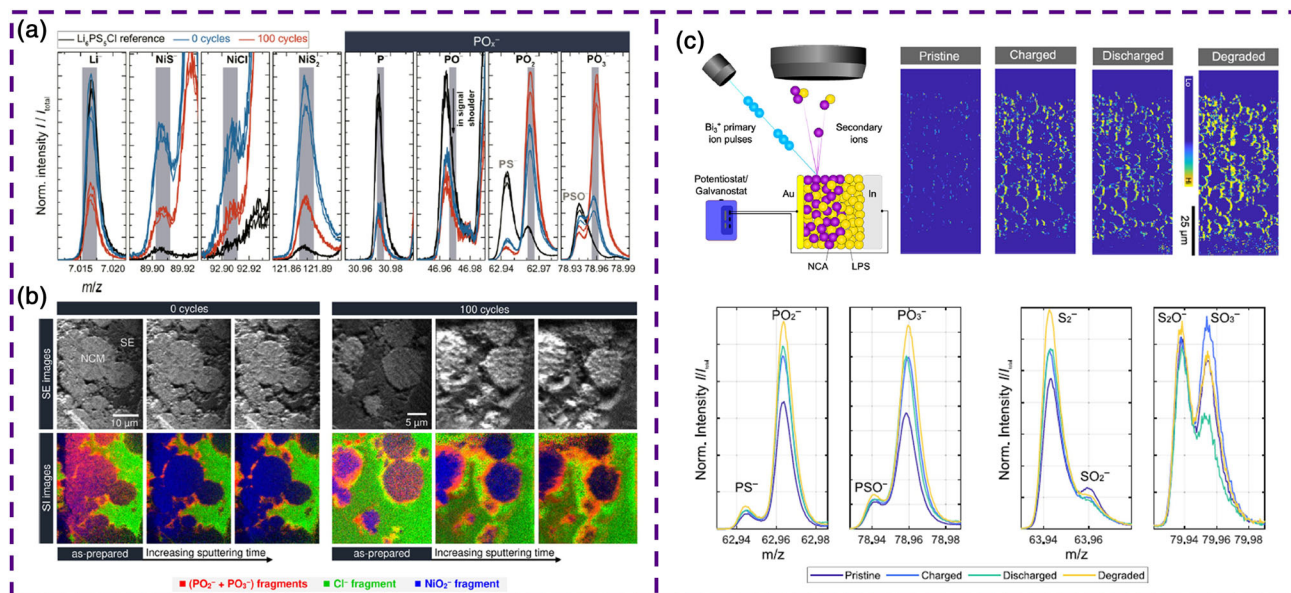


Figure 15. ToF-SIMS characterizations for analyzing the interfacial products at cathode/sulfide interfaces. a,b) Spectra of negatively charged fragments from surface of NMC622/Li₆PS₅Cl cathode composites after cycling, and secondary electron as well as corresponding secondary-ion images of the crater sidewall depending on the sputtering time. Reproduced with permission.^[87] Copyright 2019, American Chemical Society. c) Schematic illustration of operando ToF-SIMS measurement. Mass spectra and evolution of the intensity maps of PO_x⁻ and SO_x⁻ fragments measured during cell cycling. The degraded state denotes the spectra obtained with high voltage applied. Reproduced with permission.^[21] Copyright 2021, American Chemical Society.

uncycled sample), and the signals drastically increased after battery cycling (Figure 15b). Yamagishi et al.^[21] developed operando ToF-SIMS to visualize the uneven reaction of NCA cathode cycling with 75Li₂S–25P₂S₅ SEs, according to the mapping of Li-containing fragments. In addition, the authors indicated the evolution of formed PO₂⁻ and PO₃⁻ fragments after charging/discharging and degraded states. The increasing intensity of PO_x⁻ fragments accumulated at the NCA/sulfide interface suggested the irreversible interfacial reactions (Figure 15c). Janek's group further used ToF-SIMS measurements as a complementary approach to XPS analysis to reveal the interface reaction that could be aggravated upon adding carbon conductive,^[90b] while being relieved by coating Li₂CO₃/LiNbO₃ on NMC622 CAMs, according to the intensity change of detected PO_x⁻ and SO_x⁻ fragments.^[89]

3.2.5. Others (SXR, ssNMR)

Lab X-ray diffraction (XRD) is one of the most common characterizations to identify the phase composition, but it is difficult to be used to analyze the interfacial products due to the challenge of preparation of interface specimen, as well as the low concentration of interfacial products in electrodes. Synchrotron-based XRD (SXR), for example, energy-disperse XRD (EDXR), can provide high spatial resolution (spot size in micrometers), so that it can detect the interface products by scanning across the customized cell.^[98] Furthermore, the high time resolution (data acquisition in seconds) derived from the high photon flux of SR benefits to observe instantaneous interfacial evolutions with operando setups.^[69b,99] Operando SXR was always

coupled with XT to provide phase analysis and images simultaneously with the nondestructive feature, as displayed in Figure 16a. Sun et al. used this experimental apparatus to confirm the LiIn phase that penetrated through the anode interface to the bulk LGPS after cycling.^[69b] Zhu and co-workers reported using SXR to identify each component in one operating cell (Figure 16b) and then analyzed the stability of Li_{6.6}Ge_{0.6}Sb_{0.4}S₅I SEs during charging and discharging.^[99] Very recently, Bruce et al. observed the cracking and its correlation to the growth of Li dendrites within a symmetric cell (Li/Li₆PS₅Cl/Li) via using combined operando SXR and XT techniques. The SXR mapping in one 4 × 4 mm² area of the Li anode clearly indicated the location and intensity of Li dendrites that were recognized by the diffraction peak of Li (110) lattice plane (Figure 16c).^[14a] Solid-state nuclear magnetic resonance (ssNMR) spectroscopy is one powerful method to probe the chemical environments of a number of magnetically active elements. Magic angle spinning (MAS) NMR is developed to average out internal interactions of the anisotropic solids (e.g., dipolar and quadrupolar couplings between nuclei), which benefits to collect high-resolution spectra as that performed in the liquid-based NMR. Wagemaker et al. used MAS NMR to collect ³¹P NMR spectra of the C/Li₆PS₅Cl composites before and after cycling.^[11a] As displayed in Figure 16d, the deconvolution of NMR peaks suggests the formation of P₂S₇⁴⁻ and Li₃P as the interfacial products to expand the practical electrochemical window. The Li₃P-containing interface between Li metal and Li₁₀SnP₂S₁₂ was also confirmed by Yang and co-workers using ³¹P NMR.^[81]

In the physical characterizations of analyzing interfacial products, a limited number of techniques can directly detect lithium,

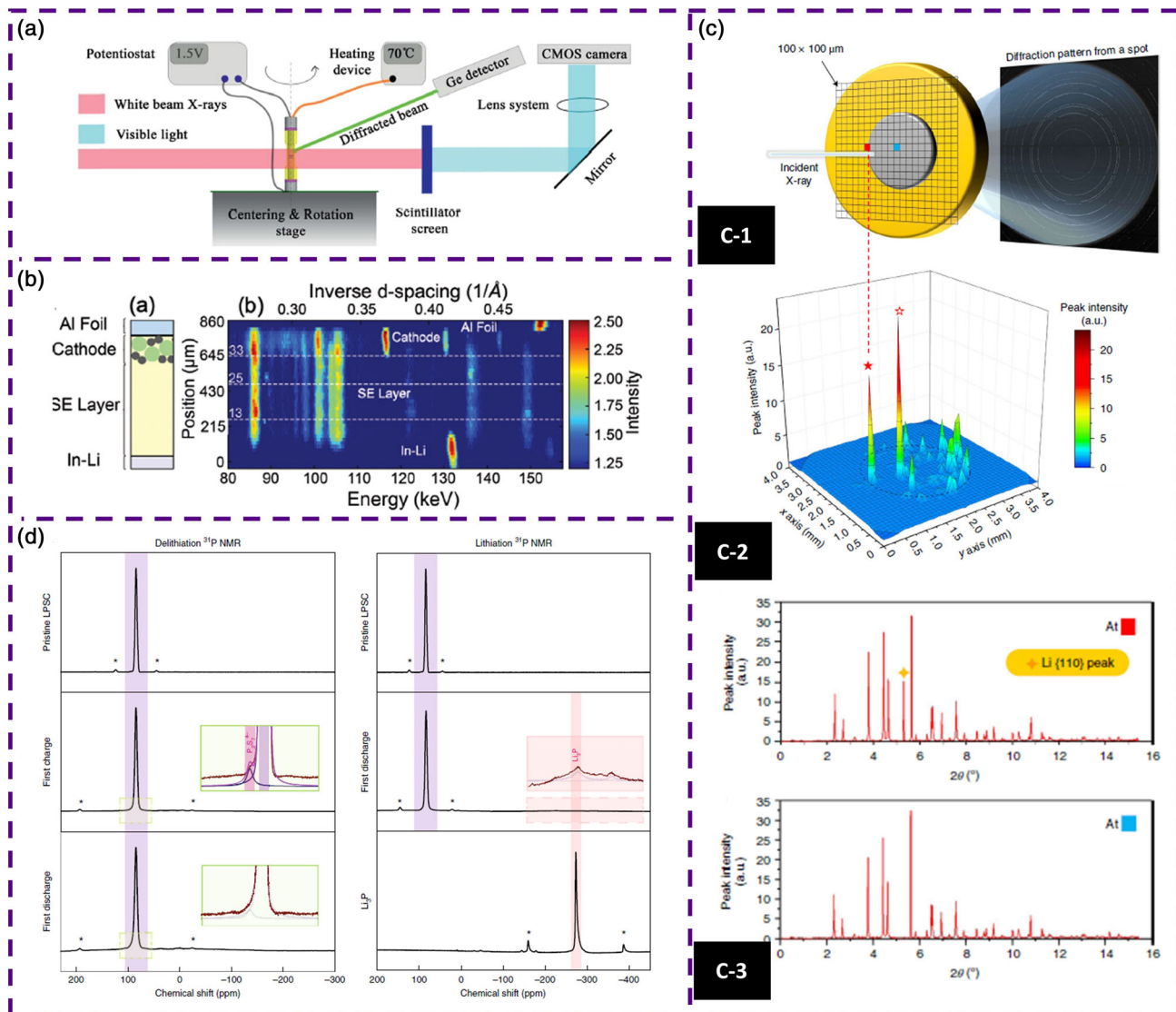


Figure 16. Other advanced characterizations to identify the interfacial products at electrode/sulfide interfaces. a) Schematic diagram of the experimental setup of the tomography station at the EDDI beam line at BESSY II, Helmholtz-Zentrum Berlin, Germany. The cell was designed for in situ/operando synchrotron XT and EDXRD. Reproduced with permission.^[69b] Copyright 2018, Royal Society of Chemistry. b) Schematic of full cell and EDXRD data of pristine full cell during electrochemical cycling in the initial state. Reproduced with permission.^[99] Copyright 2020, Wiley-VCH. c) SXR data collected on a cycled Li/Li₆PS₅Cl/Li cell after a short circuit occurred. Schematic of XRD mapping (c-1); diffraction intensity of lithium (110) peak plotted at each grid position (c-2); and XRD data collected at the edge and the center of the electrode (c-3). Reproduced with permission.^[14a] Copyright 2021, Springer Nature. d) Solid-state ³¹P NMR spectra of as-prepared, oxidized, and reduced LPSC-C. Reproduced with permission.^[11a] Copyright 2020, Springer Nature.

due to weak atomic scattering and low radiation energy for Li metal and its alloys.^[100] Auger electron spectroscopy/microscopy (AES/AEM) and atom probe tomography (APT) based on laser ablation and mass spectrometry techniques have been employed to analyze uneven Li distribution at the anode/sulfide interface and the NMC/sulfide cathode interfaces upon charging/discharging.^[101] Developments of these techniques are in the early stage to analyze electrode/sulfide interface but would play an important role to quantify Li content in the future interface studies.

4. Conclusion and Perspectives

4.1. Conclusion

Sulfide-based ASSLBs have attracted a large amount of advanced characterizations toward understanding the interfaces at both anode and cathode parts. Comparisons of representative characterization techniques are indicated in **Table 1**. At Li anode/sulfide interface, imaging techniques (e.g., OM, SEM, TEM, XT, AFM, etc.), particularly the corresponding in situ/operando

Table 1. Comparisons of representative characterization techniques in studying the electrode interfaces of sulfide-based ASSLBs.

Module and techniques		Advantages	Disadvantages
Imaging techniques	OM	Widespread	Limited spatial resolution (micrometer level)
		Relatively easy to build in situ/operando experimental apparatus	Hard-to-study cathode interface
		Suitable to observe Li dendrites	
	EM	Widespread	Potential beam damage
		High spatial resolution (down to atomic level)	Local information
		Combining imaging and spectroscopy	Challenge of interface sample preparation
		Visualizing SCL	
	XT	3D imaging can be achieved by reconstruction	
		Nondestructive	Time-consuming of 3D reconstruction
	AFM	Li metal, crack, and void can be recognized in bulk sulfide SEs	Limited spatial resolution (micrometer level)
3D imaging is a normal feature			
Widespread		Tip and sample can be damaged	
Spectroscopic investigations	XPS	Electrical properties of sample are detectable	Low scanning speed
		Widespread	Limited penetration depth (up to dozens of nanometers)
	XAS	Very surface sensitive	Poor lateral resolution
		Nondestructive	
	Raman	Depth profiling across the interface	
		High energy resolution	Scarce beamtime
		Wide range of penetration depth (depending on tunable photon energy)	SR facility is lab unattainable
	ToF-SIMS	Combined analyses in physics and chemistry	
		Depth profiling across the interface	
	SXR	Widespread	Fluorescence background
Relatively easy to build in situ/operando experimental apparatus		Potential laser radiation	
Chemical mapping			
ssNMR	High sensitivity toward ionized fragments	Potential to damage the interface	
	Identifying all elements	Identification is limited by database	
	Chemical mapping		
	Phase recognition	Scarce beamtime	
SXR	Fast acquisition (seconds)	SR facility is lab unattainable	
	High energy and nondestructive		
	Chemical mapping		
ssNMR	Li element sensitive (proton is also detectable)	Time-consuming	
	Nondestructive	Element dependent	
	Li dynamics can be quantified		

characterizations, have been elaborately developed to provide deep understandings on the growth of Li dendrites, electrolytes cracking, and electrode voiding. Spectroscopy-related methods (e.g., XPS, Raman, SXR, etc.) are used to identify the interfacial products (including the Li dendrites) derived from the reduction reaction of sulfide SEs by the Li metal anode. Importantly, these imaging and spectroscopy-related characterizations have been used complementarily to disclose the working mechanisms of some common strategies that are developed to solve the interface issues between Li metal and sulfide SEs. At the cathode side, imaging characterizations (FIB-SEM, TEM, AFM, STXM,

etc.) are employed to understand the cathode/sulfide interface problems, namely, contact loss, SCL effect, and interfacial degradations. Spectroscopy-related techniques (e.g., XPS, XAS, Raman, ToF-SIMS, etc.) clarify that the interface composition (spatial distribution and chemical structure) is a result of reduction of CAMs and oxidation of sulfide SEs during cycling. These physical characterizations are widely reported to explain the effect of the cathode coating strategies, including the morphological and chemical evolutions upon experiencing electrochemical reactions. Overall, emerging physical characterizations cannot only deepen our insights into the electrode/sulfide

interfaces, but also guide to design feasible strategies to solve interface problems, which light the way in developing high-performance and practical sulfide-based ASSLBs.

4.2. Perspectives

Although fruitful characterization methods have been well developed to understand the electrode interfaces in sulfide-based ASSLBs, several important characterizations that have emerged in other adjacent research fields are expected to be applied to deliver new insights. In addition, *in situ/operando* characterizations and a combination of imaging and spectroscopy analyses are highlighted for the future development.

4.2.1. Cryo-FIB and EM

Interfaces are highly sensitive and vulnerable, placing the acquisition of specific interface specimen as the first challenge for various characterizations, particularly for EM-related techniques that are always accompanied by electron beam damages.^[15a] Cryo-FIB and EM (including SEM and TEM) are appealed to realize unscathed observations/analyses for high-quality interface samples.^[102] SEIs derived from the electrochemical reaction between Li metal anode and LEs, as well as the cathode interface, have been studied vigorously with cryo-TEM, which refresh our understandings on the local morphology and phase composition in the interface of conventional LIBs.^[103] It is highly expected that cryo-TEM and SEM for the electrode/sulfide interface prepared by cryo-FIB bring us new insights into the interface issues at both Li anode and cathode sides. It is undeniable that the development of cryo-EM for battery science is in its infancy; various challenges are present, such as developing *in situ/operando* cryo-EM, exploring the universality of obtaining ultralow-temperature information for the ambient application, reducing data acquisition, increasing the efficiency of image reconstruction for cryo-electron tomography (cryo-ET), and so on.

4.2.2. Spallation Neutron-Related

Three spallation neutron-related techniques can be anticipated to study the electrode/sulfide interface. The first one is neutron depth profiling (NPD). This technique is used to observe the elemental Li (Li dendrites or filaments) generated in the bulk sulfide SEs, which originates from the non-negligible electronic conductivity of sulfides.^[32] In addition, NPD has been reported to reveal the interfacial behavior of garnet SEs in contact with metallic Li through *in situ* monitoring of Li plating/stripping processes.^[104] However, the distribution of Li species at the electrode/sulfide SE interface (particularly the cathode interface) has not been carefully studied by NPD. The second technique is neutron reflectometry, which measures scattering length density (SLD) as a function of depth. This method has been demonstrated to investigate SEI in LIBs using LEs, which can be transplanted to study the sulfide/electrode interfaces, particularly for the Li metal interface. The last one is neutron imaging according to the Li concentration. The spatial resolution is at the order of 100 μm but is expected to improve to 10 μm micron in the near future.^[17b]

Therefore, this technique is suitable to monitor the growth of Li dendrites initiating from the Li anode/sulfide interface.

4.2.3. Synchrotron Radiation (SR) Related

Various experimental endstations can be established by carrying the X-ray beam to go for different characterization purposes. In the review, we overviewed some SR-based techniques (X-ray imaging, absorption spectroscopy, and XRD) to study the interfaces in sulfide-based ASSLBs. Nevertheless, cutting-edge SR characterizations at the sulfide/electrode interface are expected to further show advantages in aspects of spatial, energy, and time resolutions. On the one hand, SR-related characterizations that can obtain microscopy and spectroscopy information simultaneously are needed. For example, ptychography technique derived from soft X-ray microscopy can provide high spatial resolution of several nanometers, while stacking ptychography can help to identify various interfacial products with absorption spectroscopy. This would make up for the low-energy resolution of EELS gained in TEM measurements. On the other hand, diverse *in situ/operando* SR-related characterizations should be developed. The *in situ/operando* electrochemical cell configuration is the most essential, which should be going for each SR beamline specifically. In addition, the data acquisition time should be reduced to match with the transient electrochemical reactions and interface evolutions during battery operating.

4.2.4. 2D Exchange Spectroscopy (2D EXSY) NMR

2D exchange spectroscopy (EXSY) NMR is a one of few techniques that can explore the dynamics of Li^+ transport between two different chemical sites. These two chemical sites can be two Li sites in a single material or different materials. Therefore, 2D EXSY NMR shows the capability of investigating the interfacial Li-ion migration. Wagemaker and co-workers reported using 2D EXSY NMR to illustrate the dramatically reduced Li-ion transport rates and enlarged activation energy at the interface between Li_2S and Argroditite sulfide SEs, suggesting the importance of improving ion migration at the interface for high-performance SSBs.^[105] However, there are still lack of reports utilizing 2D EXSY NMR to study interfacial ion conduction between common oxide CAMs and sulfide SEs. The application of 2D EXSY NMR is worthwhile to be extended to quantify the interfacial Li-ion dynamics in sulfide-based ASSLBs.

4.2.5. *In Situ/Operando* Characterizations

We emphasize the direction of developing *in situ/operando* characterizations to study the interface in sulfide-based SSBs. This aims at showing the significance of monitoring nature and engineering of not only interfaces, but also electrode materials and other broader research fields involving evolution in electrochemical reactions.^[106] In addition to appealing the development of *in situ/operando* in cryo-EM and SR-related techniques as shown above, researchers are encouraged to pursue every possibility of applying *in situ/operando* measurements underlying various emerging characterization methods.

4.2.6. Combination of Imaging Techniques and Spectroscopy Analyses

Characterizations on the combination of imaging techniques and spectroscopy analyses are important for researchers to study the electrode interfaces in sulfide-based ASSLBs intuitively and chemically informatively. The capability of combination has been demonstrated in 1) EDX and EELS analyses of EM, 2) component analysis of FIB–SEM reconstruction, 3) chemical recognition of STXM and MRI, and 4) multispectral imaging of Raman, ToF–SIMS, as well as synchrotron XRD. It is encouraged to make great progress with other potential techniques in this direction, such as neutron imaging, X-ray photoemission electron microscopy (XPEEM), ptychography, etc.

Acknowledgements

F.Z. and S.Z. contributed equally to this work. Y.L. acknowledges financial support from National Natural Science Foundation of China (51972219), the Collaborative Innovation Center of Suzhou Nano Science and Technology, and the 111 Project and Joint International Research Laboratory of Carbon-Based Functional Materials and Devices. X.S. acknowledges support from the Natural Sciences and Engineering Research Council of Canada (NSERC), the Canada Research Chair Program (CRC), and Western University. F.Z. acknowledges financial support from the Ontario Trillium Scholarship (OTS).

Conflict of Interest

The authors declare no conflict of interest.

Keywords

characterizations, electrode interfaces, interfacial reactions, Li dendrites, sulfide-based all-solid-state Li batteries

Received: August 13, 2021

Revised: October 24, 2021

Published online:

- [1] a) J. Janek, W. G. Zeier, *Nat. Energy* **2016**, *1*, 16141; b) R. Chen, Q. Li, X. Yu, L. Chen, H. Li, *Chem. Rev.* **2019**, *120*, 6820; c) Q. Zhao, S. Stalin, C.-Z. Zhao, L. A. Archer, *Nat. Rev. Mater.* **2020**, *5*, 229; d) G. Cui, *Matter* **2020**, *2*, 805; e) M. Li, J. Lu, Z. W. Chen, K. Amine, *Adv. Mater.* **2018**, *30*, 1800561.
- [2] a) J. W. Liang, X. N. Li, K. R. Adair, X. L. Sun, *Acc. Chem. Res.* **2021**, *54*, 1023; b) Z. Zhang, Y. Shao, B. Lotsch, Y.-S. Hu, H. Li, J. Janek, L. F. Nazar, C.-W. Nan, J. Maier, M. Armand, L. Chen, *Energy Environ. Sci.* **2018**, *11*, 1945; c) W. Zhao, J. Yi, P. He, H. Zhou, *Electrochem. Energy Rev.* **2019**, *2*, 574.
- [3] N. Kamaya, K. Homma, Y. Yamakawa, M. Hirayama, R. Kanno, M. Yonemura, T. Kamiyama, Y. Kato, S. Hama, K. Kawamoto, A. Mitsui, *Nat. Mater.* **2011**, *10*, 682.
- [4] a) Y. Kato, S. Hori, T. Saito, K. Suzuki, M. Hirayama, A. Mitsui, M. Yonemura, H. Iba, R. Kanno, *Nat. Energy* **2016**, *1*, 16030; b) Y. Kato, S. Hori, R. Kanno, *Adv. Energy Mater.* **2020**, *10*, 2002153.
- [5] a) C. Yu, F. P. Zhao, J. Luo, L. Zhang, X. L. Sun, *Nano Energy* **2021**, *83*, 105858; b) L. D. Zhou, A. Assoud, Q. Zhang, X. H. Wu, L. F. Nazar, *J. Am. Chem. Soc.* **2019**, *141*, 19002.
- [6] a) J. H. Wu, S. F. Liu, F. D. Han, X. Y. Yao, C. S. Wang, *Adv. Mater.* **2021**, *33*, 2000751; b) Q. Zhang, D. Cao, Y. Ma, A. Natan, P. Aurora, H. Zhu, *Adv. Mater.* **2019**, *31*, 1901131; c) C. H. Wang, J. W. Liang, Y. Zhao, M. T. Zheng, X. N. Li, X. L. Sun, *Energy Environ. Sci.* **2021**, *14*, 2577.
- [7] a) D. Wang, C. Zhu, Y. Fu, X. Sun, Y. Yang, *Adv. Energy Mater.* **2020**, *10*, 2001318; b) X. Yu, A. Manthiram, *Acc. Chem. Res.* **2017**, *50*, 2653; c) M. Weiss, F. J. Simon, M. R. Busche, T. Nakamura, D. Schröder, F. H. Richter, J. Janek, *Electrochem. Energy Rev.* **2020**, *3*, 221.
- [8] a) Y. Xiao, Y. Wang, S.-H. Bo, J. C. Kim, L. J. Miara, G. Ceder, *Nat. Rev. Mater.* **2019**, *5*, 105; b) S. Lou, F. Zhang, C. Fu, M. Chen, Y. Ma, G. Yin, J. Wang, *Adv. Mater.* **2021**, *33*, 2000721; c) F. Zhao, S. H. Alahakoon, K. Adair, S. Zhang, W. Xia, W. Li, C. Yu, R. Feng, Y. Hu, J. Liang, *Adv. Mater.* **2021**, *33*, 2006577; d) X.-D. Zhang, F.-S. Yue, J.-Y. Liang, J.-L. Shi, H. Li, Y.-G. Guo, *Small Struct.* **2020**, *1*, 2000042; e) J. Ma, B. B. Chen, L. L. Wang, G. L. Cui, *J. Power Sources* **2018**, *392*, 94.
- [9] A. M. Nolan, Y. Zhu, X. He, Q. Bai, Y. Mo, *Joule* **2018**, *2*, 2016.
- [10] a) L. R. Mangani, C. Villeveille, *J. Mater. Chem. A* **2020**, *8*, 10150; b) J. A. Lewis, J. Tippens, F. J. Q. Cortes, M. T. McDowell, *Trends Chem.* **2019**, *1*, 845; c) J. A. Lewis, F. J. Q. Cortes, Y. Liu, J. C. Miers, A. Verma, B. S. Vishnugopi, J. Tippens, D. Prakash, T. S. Marchese, S. Y. Han, C. Lee, P. P. Shetty, H. W. Lee, P. Shevchenko, F. De Carlo, C. Saldana, P. P. Mukherjee, M. T. McDowell, *Nat. Mater.* **2021**, *20*, 503.
- [11] a) T. K. Schwietert, V. A. Arszewska, C. Wang, C. Yu, A. Vasileiadis, N. J. J. de Klerk, J. Hageman, T. Hupfer, I. Kerkamm, Y. L. Xu, E. van der Maas, E. M. Kelder, S. Ganapathy, M. Wagemaker, *Nat. Mater.* **2020**, *19*, 428; b) Y. Zhu, X. He, Y. Mo, *ACS Appl. Mater. Interfaces* **2015**, *7*, 23685.
- [12] S. Wenzel, T. Leichtweiss, D. Kruger, J. Sann, J. Janek, *Solid State Ionics* **2015**, *278*, 98.
- [13] a) Y. Tang, L. Zhang, J. Chen, H. Sun, T. Yang, Q. Liu, Q. Huang, T. Zhu, J. Huang, *Energy Environ. Sci.* **2021**, *14*, 602; b) T. Krauskopf, F. H. Richter, W. G. Zeier, J. Janek, *Chem. Rev.* **2020**, *120*, 7745; c) P. Wang, W. Qu, W. L. Song, H. Chen, R. Chen, D. Fang, *Adv. Funct. Mater.* **2019**, *29*, 1900950.
- [14] a) Z. Ning, D. S. Jolly, G. Li, R. De Meyere, S. D. Pu, Y. Chen, J. Kasemchainan, J. Ihli, C. Gong, B. Liu, D. L. R. Melvin, A. Bonnin, O. Magdysyuk, P. Adamson, G. O. Hartley, C. W. Monroe, T. J. Marrow, P. G. Bruce, *Nat. Mater.* **2021**, DOI: 10.1038/s41563-021-00967-8; b) D. Spencer Jolly, Z. Ning, G. O. Hartley, B. Liu, D. L. R. Melvin, P. Adamson, J. Marrow, P. G. Bruce, *ACS Appl. Mater. Interfaces* **2021**, *13*, 22708.
- [15] a) Y. Cheng, L. Zhang, Q. Zhang, J. Li, Y. Tang, C. Delmas, T. Zhu, M. Winter, M.-S. Wang, J. Huang, *Mater. Today* **2021**, *42*, 137; b) H. Liu, X.-B. Cheng, J.-Q. Huang, H. Yuan, Y. Lu, C. Yan, G.-L. Zhu, R. Xu, C.-Z. Zhao, L.-P. Hou, C. He, S. Kaskel, Q. Zhang, *ACS Energy Lett.* **2020**, *5*, 833; c) K. B. Hatzell, X. C. Chen, C. L. Cobb, N. P. Dasgupta, M. B. Dixit, L. E. Marbella, M. T. McDowell, P. P. Mukherjee, A. Verma, V. Viswanathan, A. S. Westover, W. G. Zeier, *ACS Energy Lett.* **2020**, *5*, 922; d) D. Cao, X. Sun, Q. Li, A. Natan, P. Xiang, H. Zhu, *Matter* **2020**, *3*, 57.
- [16] a) C. Zheng, L. Li, K. Wang, C. Wang, J. Zhang, Y. Xia, H. Huang, C. Liang, Y. Gan, X. He, X. Tao, W. Zhang, *Batteries Supercaps* **2020**, *4*, 8; b) H.-D. Lim, J.-H. Park, H.-J. Shin, J. Jeong, J. T. Kim, K.-W. Nam, H.-G. Jung, K. Y. Chung, *Energy Storage Mater.* **2020**, *25*, 224.
- [17] a) F. Strauss, D. Kitsche, Y. Ma, J. H. Teo, D. Goonetilleke, J. Janek, M. Bianchini, T. Brezesinski, *Adv. Energy Sustainability Res.* **2021**, *2*, 2100004; b) Y. Xiang, X. Li, Y. Cheng, X. Sun, Y. Yang, *Mater. Today* **2020**, *36*, 139; c) Y. Li, Z. Gao, F. Hu, X. Lin, Y. Wei, J. Peng, J. Yang, Z. Li, Y. Huang, H. Ding, *Small Methods* **2020**, *4*, 2000111; d)

- C. Sångeland, J. Mindemark, R. Younesi, D. Brandell, *Solid State Ionics* **2019**, *343*, 115068; e) M. B. Dixit, J.-S. Park, P. Kenesei, J. Almer, K. B. Hatzell, *Energy Environ. Sci.* **2021**, DOI: 10.1039/d1ee00638j.
- [18] a) S. Wenzel, S. Randau, T. Leichtweiß, D. A. Weber, J. Sann, W. G. Zeier, *Chem. Mater.* **2016**, *28*, 2400; b) K. N. Wood, K. X. Steirer, S. E. Hafner, C. Ban, S. Santhanagopalan, S. H. Lee, G. Teeter, *Nat. Commun.* **2018**, *9*, 2490.
- [19] a) T. Hakari, M. Deguchi, K. Mitsuhashi, T. Ohta, K. Saita, Y. Orikasa, Y. Uchimoto, Y. Kowada, A. Hayashi, M. Tatsumisago, *Chem. Mater.* **2017**, *29*, 4768; b) X. Li, Z. H. Ren, M. N. Banis, S. X. Deng, Y. Zhao, Q. Sun, C. H. Wang, X. F. Yang, W. H. Li, J. W. Liang, X. N. Li, Y. P. Sun, K. Adair, R. Y. Li, Y. F. Hu, T. K. Sham, H. Huang, L. Zhang, S. G. Lu, J. Luo, X. L. Sun, *ACS Energy Lett.* **2019**, *4*, 2480.
- [20] a) L. Sang, R. T. Haasch, A. A. Gewirth, R. G. Nuzzo, *Chem. Mater.* **2017**, *29*, 3029; b) J. Zhang, C. Zheng, L. Li, Y. Xia, H. Huang, Y. Gan, C. Liang, X. He, X. Tao, W. Zhang, *Adv. Energy Mater.* **2019**, *10*, 1903311.
- [21] Y. Yamagishi, H. Morita, Y. Nomura, E. Igaki, *ACS Appl. Mater. Interfaces* **2021**, *13*, 580.
- [22] a) M. Du, K. Liao, Q. Lu, Z. Shao, *Energy Environ. Sci.* **2019**, *12*, 1780; b) A. Jena, Z. Tong, B. Bazri, K. Iputera, H. Chang, S.-F. Hu, R.-S. Liu, *J. Phys. Chem. C* **2021**, DOI: 10.1021/acs.jpcc.1c04771.
- [23] T. Fampririkis, P. Canepa, J. A. Dawson, M. S. Islam, C. Masquelier, *Nat. Mater.* **2019**, *18*, 1278.
- [24] Y. Z. Zhu, X. F. He, Y. F. Mo, *J. Mater. Chem. A* **2016**, *4*, 3253.
- [25] a) C. Monroe, J. Newman, *J. Electrochem. Soc.* **2004**, *151*, A880; b) C. Monroe, J. Newman, *J. Electrochem. Soc.* **2005**, *152*, A396.
- [26] Z. C. Liu, W. J. Fu, E. A. Payzant, X. Yu, Z. L. Wu, N. J. Dudney, J. Kiggans, K. L. Hong, A. J. Rondinone, C. D. Liang, *J. Am. Chem. Soc.* **2013**, *135*, 975.
- [27] M. Tatsumisago, M. Nagao, A. Hayashi, *J. Asian Ceram. Soc.* **2013**, *1*, 17.
- [28] K. Kerman, A. Luntz, V. Viswanathan, Y.-M. Chiang, Z. Chen, *J. Electrochem. Soc.* **2017**, *164*, A1731.
- [29] a) L. Porz, T. Swamy, B. W. Sheldon, D. Rettenwander, T. Frömling, H. L. Thaman, S. Berendts, R. Uecker, W. C. Carter, Y. M. Chiang, *Adv. Energy Mater.* **2017**, *7*, 1701003; b) A. L. Davis, R. Garcia-Mendez, K. N. Wood, E. Kazyak, K.-H. Chen, G. Teeter, J. Sakamoto, N. P. Dasgupta, *J. Mater. Chem. A* **2020**, *8*, 6291; c) E. Kazyak, R. Garcia-Mendez, W. S. LePage, A. Sharafi, A. L. Davis, A. J. Sanchez, K.-H. Chen, C. Haslam, J. Sakamoto, N. P. Dasgupta, *Matter* **2020**, *2*, 1025.
- [30] a) J. Kasemchainan, S. Zekoll, D. S. Jolly, Z. Y. Ning, G. O. Hartley, J. Marrow, P. G. Bruce, *Nat. Mater.* **2019**, *18*, 1105; b) M. B. Dixit, N. Singh, J. P. Horwath, P. D. Shevchenko, M. Jones, E. A. Stach, T. S. Arthur, K. B. Hatzell, *Matter* **2020**, *3*, 2138.
- [31] a) R. Raj, J. Wolfenstine, *J. Power Sources* **2017**, *343*, 119; b) S. Yu, D. J. Siegel, *Chem. Mater.* **2017**, *29*, 9639.
- [32] F. Han, A. Westover, J. Yue, X. Fan, F. Wang, M. Chi, D. Leonard, N. Dudney, H. Wang, C. Wang, *Nat. Energy* **2019**, *4*, 187.
- [33] a) S. Wenzel, D. A. Weber, T. Leichtweiss, M. R. Busche, J. Sann, J. Janek, *Solid State Ionics* **2016**, *286*, 24; b) J. Auvergniot, A. Cassel, D. Foix, V. Viallet, V. Seznec, R. Dedryvère, *Solid State Ionics* **2017**, *300*, 78.
- [34] L. Sang, K. L. Bassett, F. C. Castro, M. J. Young, L. Chen, R. T. Haasch, J. W. Elam, V. P. Dravid, R. G. Nuzzo, A. A. Gewirth, *Chem. Mater.* **2018**, *30*, 8747.
- [35] J. Haruyama, K. Sodeyama, L. Y. Han, K. Takada, Y. Tateyama, *Chem. Mater.* **2014**, *26*, 4248.
- [36] S. Wang, W. B. Zhang, X. Chen, D. Das, R. Ruess, A. Gautam, F. Walther, S. Ohno, R. Koerver, Q. Zhang, W. G. Zeier, F. H. Richter, C. W. Nan, J. Janek, *Adv. Energy Mater.* **2021**, *11*, 2100654.
- [37] a) Y. H. Xiao, L. J. Miara, Y. Wang, G. Ceder, *Joule* **2019**, *3*, 1252; b) S. P. Culver, R. Koerver, W. G. Zeier, J. Janek, *Adv. Energy Mater.* **2019**, *9*, 1900626; c) L. Wang, R. Xie, B. Chen, X. Yu, J. Ma, C. Li, Z. Hu, X. Sun, C. Xu, S. Dong, T. S. Chan, J. Luo, G. Cui, L. Chen, *Nat. Commun.* **2020**, *11*, 5889.
- [38] N. Ohta, K. Takada, L. Q. Zhang, R. Z. Ma, M. Osada, T. Sasaki, *Adv. Mater.* **2006**, *18*, 2226.
- [39] J. H. Woo, J. E. Trevey, A. S. Cavanagh, Y. S. Choi, S. C. Kim, S. M. George, K. H. Oh, S. H. Lee, *J. Electrochem. Soc.* **2012**, *159*, A1120.
- [40] A. Sakuda, H. Kitaura, A. Hayashi, K. Tadanaga, M. Tatsumisago, *J. Power Sources* **2009**, *189*, 527.
- [41] N. Machida, J. Kashiwagi, M. Naito, T. Shigematsu, *Solid State Ionics* **2012**, *225*, 354.
- [42] A. M. Glass, K. Nassau, T. J. Negran, *J. Appl. Phys.* **1978**, *49*, 4808.
- [43] A. L. Davis, E. Kazyak, D. W. Liao, K. N. Wood, N. P. Dasgupta, *J. Electrochem. Soc.* **2021**, *168*, 070557.
- [44] a) M. Otoyama, H. Kowada, A. Sakuda, M. Tatsumisago, A. Hayashi, *J. Phys. Chem. Lett.* **2020**, *11*, 900; b) M. Sun, T. Liu, Y. Yuan, M. Ling, N. Xu, Y. Liu, L. Yan, H. Li, C. Liu, Y. Lu, Y. Shi, Y. He, Y. Guo, X. Tao, C. Liang, J. Lu, *ACS Energy Lett.* **2021**, *6*, 451.
- [45] H. Zhou, Z. P. Luo, X. M. Li, *J. Struct. Biol.* **2019**, *205*, 59.
- [46] a) M. Nagao, A. Hayashi, M. Tatsumisago, T. Kanetsuku, T. Tsuda, S. Kuwabata, *Phys. Chem. Chem. Phys.* **2013**, *15*, 18600; b) Q. Pang, X. Liang, A. Shyamsunder, L. F. Nazar, *Joule* **2017**, *1*, 871.
- [47] S. Choi, M. Jeon, W. D. Jung, S. Yang, S. Park, H.-I. Ji, J.-H. Lee, B.-K. Kim, B.-I. Sang, H. Kim, *Solid State Ionics* **2020**, *346*, 115217.
- [48] M. Suyama, A. Kato, A. Sakuda, A. Hayashi, M. Tatsumisago, *Electrochim. Acta* **2018**, *286*, 158.
- [49] a) R. Xu, F. Han, X. Ji, X. Fan, J. Tu, C. Wang, *Nano Energy* **2018**, *53*, 958; b) F. Zhao, J. Liang, C. Yu, Q. Sun, X. Li, K. Adair, C. Wang, Y. Zhao, S. Zhang, W. Li, *Adv. Energy Mater.* **2020**, *10*, 1903422.
- [50] S. Yubuchi, M. Uematsu, C. Hotehama, A. Sakuda, A. Hayashi, M. Tatsumisago, *J. Mater. Chem. A* **2019**, *7*, 558.
- [51] a) H. Nakamura, T. Kawaguchi, T. Masuyama, A. Sakuda, T. Saito, K. Kuratani, S. Ohsaki, S. Watano, *J. Power Sources* **2020**, *448*, 227579; b) H.-T. Ren, Z.-Q. Zhang, J.-Z. Zhang, L.-F. Peng, Z.-Y. He, M. Yu, C. Yu, L. Zhang, J. Xie, S.-J. Cheng, *Rare Met.* **2021**, DOI: 10.1007/s12598-021-01804-2.
- [52] Y. Ito, M. Otoyama, A. Hayashi, T. Ohtomo, M. Tatsumisago, *J. Power Sources* **2017**, *360*, 328.
- [53] Y. Zhao, L. Zhang, J. Liu, K. Adair, F. P. Zhao, Y. P. Sun, T. P. Wu, X. X. Bi, K. Amine, J. Lu, X. L. Sun, *Chem. Soc. Rev.* **2021**, *50*, 3889.
- [54] R. Koerver, I. Aygün, T. Leichtweiß, C. Dietrich, W. Zhang, J. O. Binder, P. Hartmann, W. G. Zeier, J. Janek, *Chem. Mater.* **2017**, *29*, 5574.
- [55] X. Liu, B. Zheng, J. Zhao, W. Zhao, Z. Liang, Y. Su, C. Xie, K. Zhou, Y. Xiang, J. Zhu, H. Wang, G. Zhong, Z. Gong, J. Huang, Y. Yang, *Adv. Energy Mater.* **2021**, *11*, 2003583.
- [56] a) M. Kroll, M. Duchardt, S. L. Karstens, S. Schlabach, F. Lange, J. Hochstrasser, B. Roling, U. Tallarek, *J. Power Sources* **2021**, *505*, 230064; b) S. Choi, M. Jeon, J. Ahn, W. D. Jung, S. M. Choi, J. S. Kim, J. Lim, Y. J. Jang, H. G. Jung, J. H. Lee, B. I. Sang, H. Kim, *ACS Appl. Mater. Interfaces* **2018**, *10*, 23740; c) Y. T. Wang, J. W. Ju, S. M. Dong, Y. Y. Yan, F. Jiang, L. F. Cui, Q. L. Wang, X. Q. Han, G. L. Cui, *Adv. Funct. Mater.* **2021**, *31*, 2101523.
- [57] A. Sakuda, A. Hayashi, M. Tatsumisago, *Chem. Mater.* **2010**, *22*, 949.
- [58] W. B. Zhang, F. H. Richter, S. P. Culver, T. Leichtweiss, J. G. Lozano, C. Dietrich, P. G. Bruce, W. G. Zeier, J. Janek, *ACS Appl. Mater. Interfaces* **2018**, *10*, 22226.
- [59] H. Tsukasaki, M. Otoyama, Y. Mori, S. Mori, H. Morimoto, A. Hayashi, M. Tatsumisago, *J. Power Sources* **2017**, *367*, 42.

- [60] a) C. Wang, S. Hwang, M. Jiang, J. Liang, Y. Sun, K. Adair, M. Zheng, S. Mukherjee, X. Li, R. Li, H. Huang, S. Zhao, L. Zhang, S. Lu, J. Wang, C. V. Singh, D. Su, X. Sun, *Adv. Energy Mater.* **2021**, *11*, 2100210; b) Y. Q. Zhang, Y. Tian, Y. Xiao, L. J. Miara, Y. Aihara, T. Tsujimura, T. Shi, M. C. Scott, G. Ceder, *Adv. Energy Mater.* **2020**, *10*, 1903778.
- [61] a) A. Sakuda, A. Hayashi, T. Ohtomo, S. Hama, M. Tatsumisago, *J. Power Sources* **2011**, *196*, 6735; b) C. H. Wang, X. Li, Y. Zhao, M. N. Banis, J. W. Liang, X. N. Li, Y. P. Sun, K. R. Adair, Q. Sun, Y. L. Liu, F. P. Zhao, S. X. Deng, X. T. Lin, R. Y. Li, Y. F. Hu, T. K. Sham, H. Huang, L. Zhang, R. Yang, S. G. Lu, X. L. Sun, *Small Methods* **2019**, *3*, 1900261; c) A. Y. Kim, F. Strauss, T. Bartsch, J. H. Teo, T. Hatsukade, A. Mazilkin, J. Janek, P. Hartmann, T. Brezesinski, *Chem. Mater.* **2019**, *31*, 9664; d) L. Peng, H. Ren, J. Zhang, S. Chen, C. Yu, X. Miao, Z. Zhang, Z. He, M. Yu, L. Zhang, S. Cheng, J. Xie, *Energy Storage Mater.* **2021**, *43*, 53.
- [62] a) C. Wang, J. Liang, S. Hwang, X. Li, Y. Zhao, K. Adair, C. Zhao, X. Li, S. Deng, X. Lin, X. Yang, R. Li, H. Huang, L. Zhang, S. Lu, D. Su, X. Sun, *Nano Energy* **2020**, *72*, 104686; b) C. H. Wang, R. Z. Yu, S. Hwang, J. W. Liang, X. N. Li, C. T. Zhao, Y. P. Sun, J. W. Wang, N. Holmes, R. Y. Li, H. Huang, S. Q. Zhao, L. Zhang, S. G. Lu, D. Su, X. L. Sun, *Energy Storage Mater.* **2020**, *30*, 98.
- [63] a) Y. G. Lee, S. Fujiki, C. Jung, N. Suzuki, N. Yashiro, R. Omoda, D. S. Ko, T. Shiratsuchi, T. Sugimoto, S. Ryu, J. H. Ku, T. Watanabe, Y. Park, Y. Aihara, D. Im, I. T. Han, *Nat. Energy* **2020**, *5*, 299; b) F. Zhao, Y. Zhao, J. Wang, Q. Sun, K. Adair, S. Zhang, J. Luo, J. Li, W. Li, Y. Sun, X. Li, J. Liang, C. Wang, R. Li, H. Huang, L. Zhang, S. Zhao, S. Lu, X. Sun, *Energy Storage Mater.* **2020**, *33*, 139.
- [64] S. Deng, X. Li, Z. Ren, W. Li, J. Luo, J. Liang, J. Liang, M. N. Banis, M. Li, Y. Zhao, X. Li, C. Wang, Y. Sun, Q. Sun, R. Li, Y. Hu, H. Huang, L. Zhang, S. Lu, J. Luo, X. Sun, *Energy Storage Mater.* **2020**, *27*, 117.
- [65] D. Cao, Y. Zhang, A. M. Nolan, X. Sun, C. Liu, J. Sheng, Y. Mo, Y. Wang, H. Zhu, *Nano. Lett.* **2020**, *20*, 1483.
- [66] C.-W. Wang, F.-C. Ren, Y. Zhou, P.-F. Yan, X.-D. Zhou, S.-J. Zhang, W. Liu, W.-D. Zhang, M.-H. Zou, L.-Y. Zeng, X.-Y. Yao, L. Huang, J.-T. Li, S.-G. Sun, *Energy Environ. Sci.* **2021**, *14*, 437.
- [67] L. Wang, X. Sun, J. Ma, B. Chen, C. Li, J. Li, L. Chang, X. Yu, T. S. Chan, Z. Hu, M. Noked, G. Cui, *Adv. Energy Mater.* **2021**, <https://doi.org/10.1002/aeam.202100881>.
- [68] N. K. H. Dalasma, T. Kotaka, Y. Tabuchi, U. Pasaogullari, *ECS Trans.* **2013**, *58*, 345.
- [69] a) N. Seitzman, H. Guthrey, D. B. Sulas, H. A. S. Platt, M. Al-Jassim, S. Pylypenko, *J. Electrochem. Soc.* **2018**, *165*, A3732; b) F. Sun, K. Dong, M. Osenberg, A. Hilger, S. Risse, Y. Lu, P. H. Kamm, M. Klaus, H. Markötter, F. García-Moreno, T. Arlt, I. Manke, *J. Mater. Chem. A* **2018**, *6*, 22489.
- [70] J. M. Doux, H. Nguyen, D. H. S. Tan, A. Banerjee, X. F. Wang, E. A. Wu, C. Jo, H. D. Yang, Y. S. Meng, *Adv. Energy Mater.* **2020**, *10*, 1903253.
- [71] L. Höltschi, C. N. Borca, T. Huthwelker, F. Marone, C. M. Schlepütz, V. Pelé, C. Jordy, C. Villeveuille, M. E. Kazzi, P. Novák, *Electrochim. Acta* **2021**, *389*, 138735.
- [72] M. Otoyama, M. Suyama, C. Hotehama, H. Kowada, Y. Takeda, K. Ito, A. Sakuda, M. Tatsumisago, A. Hayashi, *ACS Appl. Mater. Interfaces* **2021**, *13*, 5000.
- [73] a) F. Han, J. Yue, X. Zhu, C. Wang, *Adv. Energy Mater.* **2018**, *8*, 1703644; b) S. J. Choi, S. H. Choi, A. D. Bui, Y. J. Lee, S. M. Lee, H. C. Shin, Y. C. Ha, *ACS Appl. Mater. Interfaces* **2018**, *10*, 31404.
- [74] M. Takahashi, T. Watanabe, K. Yamamoto, K. Ohara, A. Sakuda, T. Kimura, S. Yang, K. Nakanishi, T. Uchiyama, M. Kimura, A. Hayashi, M. Tatsumisago, Y. Uchimoto, *Chem. Mater.* **2021**, *33*, 4907.
- [75] P. H. Chien, X. Feng, M. Tang, J. T. Rosenberg, S. O'Neill, J. Zheng, S. C. Grant, Y. Y. Hu, *J. Phys. Chem. Lett.* **2018**, *9*, 1990.
- [76] J. Wan, Y. X. Song, W. P. Chen, H. J. Guo, Y. Shi, Y. J. Guo, J. L. Shi, Y. G. Guo, F. F. Jia, F. Y. Wang, R. Wen, L. J. Wan, *J. Am. Chem. Soc.* **2021**, *143*, 839.
- [77] M. Otoyama, T. Yamaoka, H. Ito, Y. Inagi, A. Sakuda, M. Tatsumisago, A. Hayashi, *J. Phys. Chem. C* **2021**, *125*, 2841.
- [78] a) S. M. Zhang, F. P. Zhao, S. Wang, J. W. Liang, J. Wang, C. H. Wang, H. Zhang, K. Adair, W. H. Li, M. S. Li, H. Duan, Y. Zhao, R. Z. Yu, R. Y. Li, H. Huang, L. Zhang, S. Q. Zhao, S. G. Lu, T. K. Sham, Y. F. Mo, X. L. Sun, *Adv. Energy Mater.* **2021**, *11*, 2100836; b) W. H. Li, Z. Q. Wang, F. P. Zhao, M. S. Li, X. J. Gao, Y. Zhao, J. Wang, J. G. Zhou, Y. F. Hu, Q. F. Xiao, X. Y. Cui, M. J. Eslamibidgoli, M. H. Eikerling, R. Y. Li, F. Brandys, R. Divigalpitiya, T. K. Sham, X. L. Sun, *Chem. Mater.* **2020**, *32*, 1272.
- [79] a) A. Kato, H. Kowada, M. Deguchi, C. Hotehama, A. Hayashi, M. Tatsumisago, *Solid State Ionics* **2018**, *322*, 1; b) M. Suyama, S. Yubuchi, M. Deguchi, A. Sakuda, M. Tatsumisago, A. Hayashi, *J. Electrochem. Soc.* **2021**, *168*, 060542.
- [80] S. Wenzel, S. J. Sedlmaier, C. Dietrich, W. G. Zeier, J. Janek, *Solid State Ionics* **2018**, *318*, 102.
- [81] B. Z. Zheng, X. S. Liu, J. P. Zhu, J. Zhao, G. M. Zhong, Y. X. Xiang, H. C. Wang, W. M. Zhao, E. Umeshbabu, Q. H. Wu, J. Y. Huang, Y. Yang, *Nano Energy* **2020**, *67*, 104252.
- [82] Y. Gao, D. W. Wang, Y. G. C. Li, Z. X. Yu, T. E. Mallouk, D. H. Wang, *Angew. Chem. Int. Ed.* **2018**, *57*, 13608.
- [83] F. Zhao, Q. Sun, C. Yu, S. Zhang, K. Adair, S. Wang, Y. Liu, Y. Zhao, J. Liang, C. Wang, X. Li, X. Li, W. Xia, R. Li, H. Huang, L. Zhang, S. Zhao, S. Lu, X. Sun, *ACS Energy Lett.* **2020**, *5*, 1035.
- [84] J. Liang, X. Li, Y. Zhao, L. Goncharova, W. Li, K. Adair, M. Banis, Y. Hu, T. Sham, H. Huang, L. Zhang, S. Zhao, S. Lu, R. Li, X. Sun, *Adv. Energy Mater.* **2019**, *9*, 1902125.
- [85] S. H. Jung, K. Oh, Y. J. Nam, D. Y. Oh, P. Brüner, K. Kang, Y. S. Jung, *Chem. Mater.* **2018**, *30*, 8190.
- [86] J. Auvergniot, A. Cassel, J.-B. Ledeuil, V. Viallet, V. Seznec, R. Dedryvère, *Chem. Mater.* **2017**, *29*, 3883.
- [87] F. Walther, R. Koerver, T. Fuchs, S. Ohno, J. Sann, M. Rohnke, W. G. Zeier, J. Janek, *Chem. Mater.* **2019**, *31*, 3745.
- [88] A. Banerjee, H. M. Tang, X. F. Wang, J. H. Cheng, H. Nguyen, M. H. Zhang, D. H. S. Tang, T. A. Wynn, E. A. Wu, J. M. Doux, T. P. Wu, L. Ma, G. E. Sterbinsky, M. S. D'Souza, S. P. Ong, Y. S. Meng, *ACS Appl. Mater. Interfaces* **2019**, *11*, 43138.
- [89] F. Walther, F. Strauss, X. Wu, B. Mogwitz, J. Hertle, J. Sann, M. Rohnke, T. Brezesinski, J. Janek, *Chem. Mater.* **2021**, *33*, 2110.
- [90] a) K. Yoon, J. J. Kim, W. M. Seong, M. H. Lee, K. Kang, *Sci. Rep.* **2018**, *8*, 8066; b) F. Walther, S. Randau, Y. Schneider, J. Sann, M. Rohnke, F. H. Richter, W. G. Zeier, J. Janek, *Chem. Mater.* **2020**, *32*, 6123; c) F. Strauss, D. Stepien, J. Maibach, L. Pfaffmann, S. Indris, P. Hartmann, T. Brezesinski, *RSC Adv.* **2020**, *10*, 1114; d) S. X. Deng, Y. P. Sun, X. Li, Z. H. Ren, J. W. Liang, K. Doyle-Davis, J. N. Liang, W. H. Li, M. N. Banis, Q. Sun, R. Y. Li, Y. F. Hu, H. Huang, L. Zhang, S. G. Lu, J. Luo, X. L. Sun, *ACS Energy Lett.* **2020**, *5*, 1243.
- [91] F. Lin, Y. J. Liu, X. Q. Yu, L. Cheng, A. Singer, O. G. Shpyrko, H. L. L. Xing, N. Tamura, C. X. Tian, T. C. Weng, X. Q. Yang, Y. S. Meng, D. Nordlund, W. L. Yang, M. M. Doeff, *Chem. Rev.* **2017**, *117*, 13123.
- [92] K. Chen, K. Yamamoto, Y. Orikasa, T. Uchiyama, Y. Ito, S. Yubuchi, A. Hayashi, M. Tatsumisago, K. Nitta, T. Uruga, Y. Uchimoto, *Solid State Ionics* **2018**, *327*, 150.
- [93] S. Deng, Q. Sun, M. Li, K. Adair, C. Yu, J. Li, W. Li, J. Fu, X. Li, R. Li, Y. Hu, N. Chen, H. Huang, L. Zhang, S. Zhao, S. Lu, X. Sun, *Energy Storage Mater.* **2021**, *35*, 661.

- [94] P. J. Hendra, C. J. Vear, *Analyst* **1970**, 95, 321.
- [95] Y. Zhou, C. Doerr, J. Kasemchainan, P. G. Bruce, M. Pasta, L. J. Hardwick, *Batteries Supercaps* **2020**, 3, 647.
- [96] M. Otoyama, Y. Ito, A. Hayashi, M. Tatsumisago, *J. Power Sources* **2016**, 302, 419.
- [97] a) X. Li, H. Guan, Z. Ma, M. Liang, D. Song, H. Zhang, X. Shi, C. Li, L. Jiao, L. Zhang, *J. Energy Chem.* **2020**, 48, 195; b) G. Lu, X. Li, Z. Wang, D. Song, H. Zhang, C. Li, L. Zhang, L. Zhu, *J. Power Sources* **2020**, 468, 228372.
- [98] Q. Zhang, A. M. Bruck, D. C. Bock, J. Li, V. Sarbada, R. Hull, E. A. Stach, K. J. Takeuchi, E. S. Takeuchi, A. C. Marschilok, *Phys. Chem. Chem. Phys.* **2017**, 19, 14160.
- [99] X. Sun, A. M. Stavola, D. Cao, A. M. Bruck, Y. Wang, Y. Zhang, P. Luan, J. W. Gallaway, H. Zhu, *Adv. Energy Mater.* **2020**, 11, 2002861.
- [100] a) Y. Shao-Horn, L. Croguennec, C. Delmas, E. C. Nelson, M. A. O'Keefe, *Nat. Mater.* **2003**, 2, 464; b) P. Hovington, V. Timoshevskii, S. Burgess, H. Demers, P. Statham, R. Gauvin, K. Zaghib, *Scanning* **2016**, 38, 571.
- [101] a) S. H. Kim, K. Kim, H. Choi, D. Im, S. Heo, H. S. Choi, *J. Mater. Chem. A* **2019**, 7, 13650; b) S. Choi, B.-N. Yun, W. D. Jung, T. H. Kim, K.-Y. Chung, J.-W. Son, B.-I. Sang, H.-G. Jung, H. Kim, *Scr. Mater.* **2019**, 165, 10.
- [102] a) Y. B. Li, W. Huang, Y. Z. Li, W. Chiu, Y. Cui, *Acs Nano* **2020**, 14, 9263; b) Z. Ju, H. Yuan, O. Sheng, T. Liu, J. Nai, Y. Wang, Y. Liu, X. Tao, *Small Sci.* **2021**, DOI: 10.1002/smssc.202100055; c) M. J. Zachman, Z. Y. Tu, S. Choudhury, L. A. Archer, L. F. Kourkoutis, *Nature* **2018**, 560, 345.
- [103] a) Z. W. Zhang, J. L. Yang, W. Huang, H. S. Wang, W. J. Zhou, Y. B. Li, Y. Z. Li, J. W. Xu, W. X. Huang, W. Chiu, Y. Cui, *Matter* **2021**, 4, 302; b) Y. Z. Li, Y. B. Li, A. L. Pei, K. Yan, Y. M. Sun, C. L. Wu, L. M. Joubert, R. Chin, A. L. Koh, Y. Yu, J. Perrino, B. Butz, S. Chu, Y. Cui, *Science* **2017**, 358, 506; c) C.-Y. Chen, T. Tsuda, Y. Oshima, S. Kuwabata, *Small Struct.* **2021**, 2, 2100018; d) G. J. Yang, S. M. Zhang, S. T. Weng, X. Y. Li, X. F. Wang, Z. X. Wang, L. Q. Chen, *Nano Lett.* **2021**, 21, 5316.
- [104] C. W. Wang, Y. H. Gong, J. Q. Dai, L. Zhang, H. Xie, G. Pastel, B. Y. Liu, E. Wachsman, H. Wang, L. B. Hu, *J. Am. Chem. Soc.* **2017**, 139, 14257.
- [105] a) C. Yu, S. Ganapathy, E. Eck, H. Wang, S. Basak, Z. Li, M. Wagemaker, *Nat. Commun.* **2017**, 8, 1086; b) C. Yu, S. Ganapathy, N. J. J. de Klerk, I. Roslon, E. R. H. van Eck, A. P. M. Kentgens, M. Wagemaker, *J. Am. Chem. Soc.* **2016**, 138, 11192.
- [106] a) J. Li, G. Johnson, S. Zhang, D. Su, *Joule* **2019**, 3, 4; b) A. M. Tripathi, W. N. Su, B. J. Hwang, *Chem. Soc. Rev.* **2018**, 47, 736; c) Q. F. Gu, J. A. Kimpton, H. E. A. Brand, Z. Y. Wang, S. L. Chou, *Adv. Energy Mater.* **2017**, 7, 1602831.
- [107] Y. Seino, T. Ota, K. Takada, A. Hayashi, M. Tatsumisago, *Energy Environ. Sci.* **2014**, 7, 627.
- [108] F. Mizuno, A. Hayashi, K. Tadanaga, M. Tatsumisago, *Adv. Mater.* **2005**, 17, 918.
- [109] J. H. Kennedy, Z. M. Zhang, H. Eckert, *J. Non-Cryst. Solids* **1990**, 123, 328.
- [110] C. Dietrich, D. A. Weber, S. J. Sedlmaier, S. Indris, S. P. Culver, D. Walter, J. Janek, W. G. Zeier, *J. Mater. Chem. A* **2017**, 5, 18111.
- [111] P. Bron, S. Johansson, K. Zick, J. S. auf der Gunne, S. Dehnen, B. Roling, *J. Am. Chem. Soc.* **2013**, 135, 15694.
- [112] J. M. Whiteley, J. H. Woo, E. Y. Hu, K. W. Nam, S. H. Lee, *J. Electrochem. Soc.* **2014**, 161, A1812.
- [113] P. Adeli, J. D. Bazak, K. H. Park, I. Kochetkov, A. Huq, G. R. Goward, L. F. Nazar, *Angew. Chem. Int. Edit.* **2019**, 58, 8681.
- [114] M. A. Kraft, S. Ohno, T. Zinkevich, R. Koerver, S. P. Culver, T. Fuchs, A. Senyshyn, S. Indris, B. J. Morgan, W. G. Zeier, *J. Am. Chem. Soc.* **2018**, 140, 16330.
- [115] H. J. Deiseroth, S. T. Kong, H. Eckert, J. Vannahme, C. Reiner, T. Zais, M. Schlosser, *Angew. Chem. Int. Ed.* **2008**, 47, 755.
- [116] E. Rangasamy, Z. C. Liu, M. Gobet, K. Pilar, G. Sahu, W. Zhou, H. Wu, S. Greenbaum, C. D. Liang, *J. Am. Chem. Soc.* **2015**, 137, 1384.
- [117] T. Kaib, S. Haddadpour, M. Kapitein, P. Bron, C. Schröder, H. Eckert, B. Roling, S. Dehnen, *Chem. Mater.* **2012**, 24, 2211.



Feipeng Zhao is a postdoctoral associate (PDA) at Western University. He received his Ph.D. in mechanical and materials engineering from Western University, Canada, in August 2021. He obtained his B.S. and M.S. in materials science from Soochow University in 2014 and 2017, respectively. He is working on the synthesis and characterizations of advanced inorganic solid-state electrolytes and interfaces for high-performance all-solid-state batteries.



Shumin Zhang is a Ph.D. candidate in Professor Xueliang (Andy) Sun's Group at Western University, Canada. She received his B.S. and M.S. in materials science from Soochow University in 2016 and 2019, respectively. Currently, her research focuses on the synthesis and characterization of sulfide and halide electrolytes, as well as development of high-performance all-solid-state Li/Na metal batteries.



Yanguang Li is a professor at the Institute of Functional Nano & Soft Materials (FUNSOM) of Soochow University, China. He received his B.S. in chemistry from Fudan University, China, in 2005 and obtained his Ph.D. in chemistry from Ohio State University in 2010. He then moved to the Stanford University and completed the postdoctoral training before taking the current faculty position in 2013. His research focuses on nanostructured functional materials for energy applications, in the realm of advanced materials, electrocatalysis, and photocatalysis.



Xueliang (Andy) Sun is a Canada Research Chair in Development of Nanomaterials for Clean Energy, Fellow of the Royal Society of Canada and Canadian Academy of Engineering and Full Professor at Western University, Canada. Dr. Sun received his Ph.D. in materials chemistry in 1999 from the University of Manchester, UK, which he followed up by working as a postdoctoral fellow at the University of British Columbia, Canada and as a Research Associate at L'Institut National de la Recherche Scientifique (INRS), Canada. His current research interests focus on advanced materials for lithium-ion batteries, metal–air batteries, and fuel cells.